The Role of Crystalline Imperfections on the Thermal Conductivity of Functional Oxide Thin Films

---

A thesis presented to

the faculty of the School of Engineering and Applied Science

University of Virginia

---

in partial fulfillment

of the requirements for the degree of

Master of Science in Materials Science and Engineering

by

Kelsey E. Meyer

May 2017

The Role of Crystalline Imperfections on the Thermal Conductivity of Functional Oxide Thin Films

by

Kelsey E. Meyer

Abstract

Understanding nanoscale thermal transport in functional oxide thin films is critical for a wide variety of applications. In particular, these materials are frequently used as gate dielectrics and insulating buffers in electronic and thermoelectric devices. Given the imperfect structural nature of most functional materials, it is critical to understand how defects, dislocations, and varying degrees of crystalline disorder impact thermal transport in oxide thin films. This work attempts to contribute to this body of knowledge by focusing on two main studies.

First, we consider the effect of defects on thermal conductivity. Phonon scattering in crystalline systems can be strongly dictated by a wide array of defects, many of which can be difficult to observe via standard microscopy techniques. We experimentally demonstrate that the phonon thermal conductivity of MgO thin films is proportional to the crystal coherence length, a property of a solid that quantifies the length scale associated with crystalline imperfections. Sputter deposited films were prepared on (100) silicon and then annealed to vary the crystalline coherence, as characterized using x-ray diffraction line broadening. We find that the measured thermal conductivity of the MgO films varies proportionally with crystal coherence length, which is ultimately limited by the grain size. The microstructural length scales associated with crystalline defects, such as small angle tilt boundaries, dictate this crystalline coherence length and our results demonstrate the role that this length scale plays on the phonon thermal conductivity of thin films. Our results suggest

that this crystalline coherence length scale provides a measure of the limiting phonon mean free path in crystalline solids, a quantity that is often difficult to measure and observe with more traditional imaging techniques.

Second, we study density and length scale effects in amorphous thin films. We measure the room temperature thermal conductivity of atomic layer deposition-grown amorphous Al_2O_3 and TiO_2 thin films as a function of film thickness and atomic density. For films thinner than 50 nm, we measure an effective thermal conductivity that is reduced with decreasing film thickness. This dependence is attributed to the increased influence of thermal boundary resistances as film thickness is reduced. In addition, we fit for a thickness-independent intrinsic thermal conductivity using a series-resistor model. For films thicker than ~50 nm, there is no significant dependence on thickness or substrate. We observe a strong density dependence of the thermal conductivity, which agrees well with a differential effective-medium approximation modified with a minimum limit model.

Table of Contents

List of Figures

List of Tables

Chapter 1

Introduction

1.1 Applications

Transistors are extremely important semiconductor devices used in the world of microelectronics. Not only can they provide amplification of electrical signals, they often serve as switching devices.[1–3] Metal-oxide-semiconductor field-effect transistors, or MOSFET's, are a particularly important example of these devices. One type of MOSFET (illustrated in Fig. 1.1) is built by embedding small regions of a p-type semiconductor within an n-type substrate. These regions are connected via a thin p-type channel. Metal contacts are deposited onto these regions, and act as a source and a drain. An insulating layer, the gate dielectric, is grown on the exposed p-type semiconductor; a metal electrode, or the gate electrode, is then deposited on the surface of this dielectric layer. A MOSFET operates by imposing an electric field on the gate via application of a voltage to the gate electrode. This applied field drives charge carriers out of the channel, changing its electrical conductivity; a small change in field at the gate creates a relatively large variation in current between the source and drain contacts.[2, 3]

In silicon-based MOSFET's, an insulating layer of silicon dioxide is often used as

the gate dielectric since it can be easily grown via oxidation of the silicon surface.[3] However, silicon dioxide has a fairly low relative permittivity (k ~ 4)[2,3] and thermal conductivity (k ~ 1.4 $Wm^{-1}K^{-1}$),[3,4] which can limit the operating power; in addition, depending on the semiconductor used, it is not necessarily compatible in all MOSFET devices. When fabricating these transistors and determining an appropriate gate dielectric, there are a large number of factors to consider: the relative permittivity and band gap; film microstructure; interfacial quality; compatibility between the semiconductor and metals in the structure; processing limitations; and reliability.[5]

Many different high k oxide thin films have been studied for use as gate dielectrics; of particular relevance to this work, thin films of Al_2O_3, TiO_2, and MgO have all been investigated for potential use as gate dielectrics in MOSFET devices. The dielectric constants of Al_2O_3, TiO_2, and MgO are ~10, ~80, and ~8, respectively.[6–12] While many dielectrics are crystalline, amorphous oxide thin films are of particular interest for use as gate dielectrics because unlike crystalline materials, they lack grain boundaries that can act as a source of current leakage.[5]

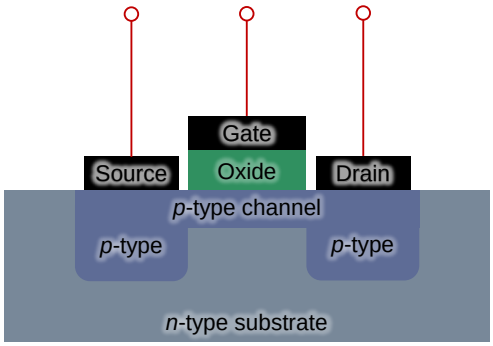

Figure 1.1: Schematic of a depletion-mode p-type MOSFET device.

The oxides studied in this thesis are thermal insulators that are of interest for a wide array of technologies beyond gate dielectrics, since they can be deposited at low temperatures,[13, 14] are biologically stable,[13] and chemically inert.[15–18] Amorphous Al_2O_3 is one of the most widely studied ALD grown materials[19–27] and has received considerable attention for its excellent optical, chemical, and mechanical prop-

erties.[28] It is used in optical lenses and windows, refractory coatings, antireflection coatings,[29–31] optical wave guides,[32–35] anticorrosive coatings,[36–38] humidity sensors,[39] and as a heat sink in integrated circuits.[40] Amorphous TiO_2 has been studied for use as an optical coating and in sub-wavelength optical structures due to its relatively high refractive index.[41–45] It is also of interest as an anticorrosive coating[46] and is often used in solar cells[47–49] and electrical switching devices.[50, 51] Finally, MgO has a relatively large band gap and is thermally stable.[52] It is often used as an oxide barrier in various microelectronic devices.[53, 54]

1.2 Statement of Objectives

The major objective of this work is to understand thermal transport in disordered oxide films. As discussed in more detail in the following chapter, the degree of disorder in a material can range quite significantly, from near-perfect single crystals to crystalline systems with sub-micron defects and completely disordered amorphous materials. This work focuses on materials in the last two categories: MgO with varied levels of defects and dislocations, and amorphous Al_2O_3 and TiO_2 of varying film thickness and density. Because most materials possess some degree of disorder, it is crucial to understand how this impacts their thermal properties when designing any type of device. The remainder of this thesis is outlined as follows:

Chapter 2 discusses the basic concepts used throughout this thesis. The idea of phonons and the mathematical description of phonon thermal conductivity are defined. Furthermore, the types of defects present in crystalline materials that impede phonon thermal transport are discussed.

Chapter 3 introduces time-domain thermoreflectance (TDTR), the experiment used to measure all of the thermal properties discussed in this work. TDTR is a non-contact optical thermometry technique that is well suited for measuring thermal

properties of thin films.

Chapter 4 explores the concept of the crystalline coherence length, a microstructural parameter governed by sub-grain dislocations and other defects, and the effect this has on phonon scattering and the thermal conductivity of magnesium oxide thin films. The thermal conductivity is found to vary significantly with crystalline coherence length, highlighting the role that dislocations and other defects play in phonon scattering.

Chapter 5 discusses density and length scale effects in amorphous alumina and titania thin films. A strong density dependence of the thermal conductivity is observed, which agrees well with a differential effective-medium approximation modified with a minimum limit model.

Chapter 6 summarizes the major findings of this thesis and suggests potential future directions in which this work could continue.

Chapter 2

Background

This chapter will outline the general concepts and theory underlying the work discussed in later chapters.

2.1 Defects in Crystalline Materials

A material is said to be crystalline if it possesses long-range, periodic order. While nearly-perfect single crystals can be grown, most bulk materials and thin films contain a wide variety of defects. These are typically divided into categories of point, line, planar, and volume defects. Point defects are zero-dimensional, because they only occur on or near a lattice site. Line defects are one-dimensional, in the sense that they are lines through the crystal along which crystallographic registry is lost, while planar defects are two-dimensional. Finally, volume defects are considered three-dimensional.[3]

There are several types of point defects, all of which are shown schematically in Figure 2.1. Interstitials occur when an atom occupies a space in the crystal that is not normally occupied; this can take the form of two atoms sharing a lattice site or an impurity atom occupying a site between lattice atoms. In contrast, a vacancy is a point defect in which an atom is missing from a lattice site. Schottky defects[55] occur

in ionic materials, when an equal number of anions and cations are vacant from their lattice sites such that electrical neutrality and stoichiometry are maintained. Frenkel pairs[56] are combinations of interstitials and vacancies: an atom is displaced from its lattice site and occupies a previously empty space in the lattice, leaving behind a vacancy and becoming an interstitial. Nearly all crystalline materials contain point defects.[3]

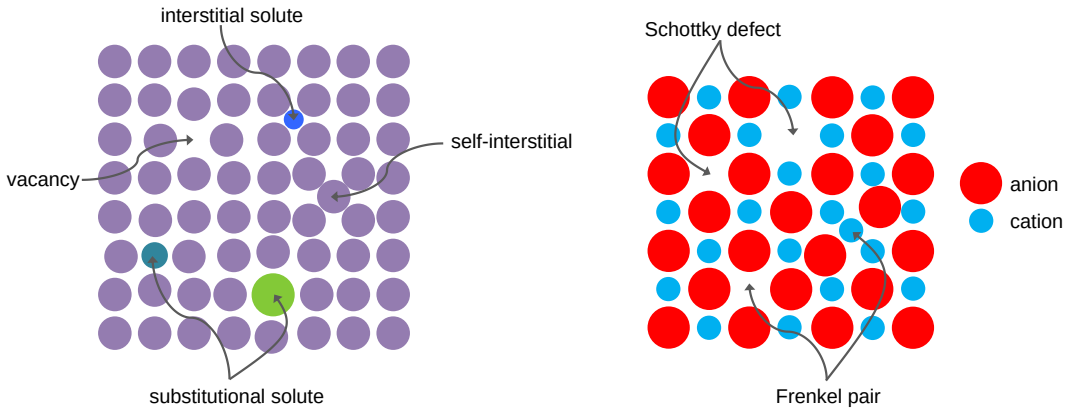

Figure 2.1: Schematic of various types of point defects.

The most notable examples of line defects are edge and screw dislocations and combinations of both, called mixed dislocations. Edge dislocations occur when an additional partial plane of atoms is introduced into the crystal, distorting the rest of the lattice, as illustrated in Figure 2.2. Screw dislocations are similar and have a spiral nature, also shown in Figure 2.2. Both types of dislocations are typically quantified using the Burgers vector, $\mathbf{b}$, which indicates the magnitude and direction of lattice distortion associated with the dislocation. The nature of the dislocation is defined by the relative orientations of the dislocation line and the Burgers vector[57]: for an edge dislocation, they are perpendicular, while for a screw they are parallel. In most materials, the Burgers vector has a magnitude equal to the lattice spacing and points in a close-packed crystallographic direction. Dislocations are relatively

difficult to observe experimentally but have been discerned via transmission electron microscopy, x-ray topography, field ion emission, and atom probe techniques.[3] An example of dislocations observed via TEM is shown in Figure 2.3(a). Planar defects

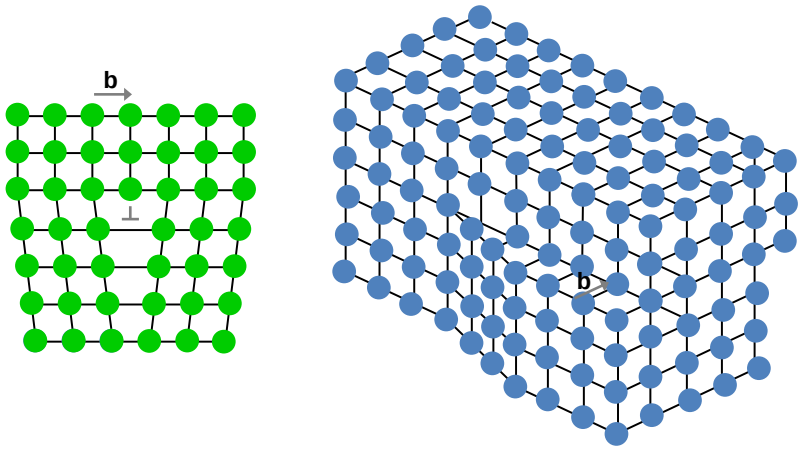

Figure 2.2: Schematic of edge (left) and screw (right) dislocations.

are two dimensional and include grain boundaries, twin boundaries, and stacking faults. Grain boundaries are interfaces between grains of varying orientations in polycrystalline materials; one example of grain boundaries in a thin film is shown in Figure 2.3(b). Low angle-tilt boundaries occur between grains that are mis-oriented at relatively small angles (typically $<15°$). Twin boundaries are interfaces between two crystals with similar symmetries, resulting in minor mis-orientation between the crystallites. Stacking faults are interruptions between differently stacked layers and disrupt lattice periodicity.[3]

Volume defects are most common in bulk materials, and so are less relevant to the thin films studied in this work; these include pores, voids, precipitates, inclusions, dispersants, and cracks.[3]

Having introduced the varieties of defects that are typically present in materials, it is important to define the crystalline coherence length, the characteristic length scale of a crystal that is devoid of translational symmetry-breaking defects.[58] That is, the coherence length is dictated by sub-grain dislocations and defects, and this

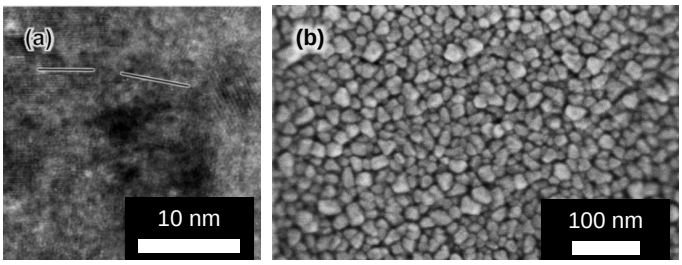

Figure 2.3: (a) High-resolution TEM image of an MgO thin film, where the lines highlight (200)-type planes for adjacent grains (taken from Ref. [58]); (b) SEM image of grains in a similarly processed MgO film (taken from Ref. [59]).

length scale is limited by the grain size. This length scale can be quantified relatively easily using x-ray diffraction.

While all materials possess a certain degree of defects, crystalline materials still maintain their long-range order and atomic periodicity; in contrast, amorphous materials are nearly completely disordered. This distinction is discussed in more detail in Section 2.3 and is relevant to the materials studied in this thesis.

2.2 Phonons

The concept of phonons and the scientific breakthroughs leading to their discovery has a long history. In 1907, Einstein proposed his theory of what would later be known as an Einstein solid: he theorized that each atom in a solid could be modeled as an independent, three-dimensional quantum harmonic oscillator vibrating at the same frequency[60], and later applied his theory to predict the thermal conductivity of crystalline solids.[61] While his model explained the temperature-dependent specific heat observed by Weber previously,[62,63] it did not completely capture the trends at low temperatures. This is because, at temperatures approaching zero, his calculated specific heat decreased exponentially, a result that arises due to the assumption that all oscillations occur at the same frequency. Debye later rectified this by quantizing the normal modes of the solid,[64] determining a T^3 dependence at low temperatures

that is consistent with experimental measurements. However, it is worth noting that even today, a modified version of Einstein's model describes the thermal conductivity trends in amorphous, porous, and otherwise heavily disordered materials fairly well, as discussed in more detail later in this chapter.

While Einstein and Debye had used the quantization of the energy of elastic vibrations to describe the heat capacities of solids, the theory of potential carriers associated with these vibrations came later. Using Dirac's advanced theories of quantization[65], Tamm developed the idea of quanta of elastic oscillations as an analogy to Einstein's "light quantum" in 1930.[66] Soon after this, Frenkel discussed the concept in his 1932 textbook[67] and suggested the name "phonon" to describe these vibrational modes.[1]

More formally, a phonon is an excitation associated with the quantized energy of a lattice vibration.[1, 67, 68] In crystalline materials, collective oscillations of atoms around their equilibrium positions give rise to elastic waves which propagate across the crystal, and particularly in nonmetallic solids, phonons are the predominant carrier of thermal energy.

In a three-dimensional crystal with N atoms, there are $3N$ phonon modes with three different polarizations, two transverse and one longitudinal. Transverse modes are perpendicular deviations from the atomic equilibrium position with respect to the direction of propagation, while longitudinal waves are deviations that are parallel to the propagation direction. The type of phonon modes present in a material is dependent on the bonding characteristics and masses of the constituent atoms, along with lattice and basis of the crystal.[1, 68]

[1]Interestingly, Frenkel's text dismisses the idea of phonons as being anything other than fictitious, noting in a footnote that:

> "It is not in the least intended to convey hereby the impression that such phonons have a real existence. On the contrary, the possibility of their introduction rather serves to discredit the belief in the real existence of photons."

Depending on the material, different phonon branches may exist and are categorized according to their nature and frequencies. Acoustic phonons are lower frequency vibrational modes. At the zone center, the atoms in the unit cell vibrate in phase; this is characteristic of sound wave (hence the origin of the term "acoustic" branch). In monatomic crystals only acoustic modes are present; if a crystal has more than one atom in its basis, optical phonons will also exist. These are higher frequency modes with more out of phase oscillations between the basis atoms as compared to the acoustic modes. If these atoms had opposite charges, this mode of vibration could be excited by an electric field; in an ionic crystal, this field is associated with the infrared portion of the visible spectrum of light (hence the origin of the term "optical" branch).[68]

These concepts are well illustrated by phonon dispersion curves, which relate the phonon frequency to the wavevector. The slope of these curves gives the group velocity of phonon propagation, $v_{\mathrm{j}} = \partial\omega_{\mathrm{j}}/\partial\hbar k$, where $\hbar k = 2\pi/\lambda$ is the wavevector, λ is the phonon wavelength, and j is the phonon branch. Examples of phonon dispersion for a simple monatomic system (gold, face-centered cubic structure or space group $Fm\bar{3}m$), a cubic structure with a two atom basis (MgO, rocksalt structure or Fm3m), and a more complex hexagonal unit cell (sapphire, $R\bar{3}c$) are shown in Fig 2.4. Information about the phonon dispersion in a crystal can enable calculation of the thermal conductivity. From the kinetic theory of solids, the thermal conductivity can be written as:

$$\kappa = \frac{1}{3}\sum_{j}\int_{0}^{\omega_{c,j}} C_j(\omega)v_j(\omega)\lambda_j(\omega)d\omega = \frac{1}{3}\sum_{j}\int_{0}^{\omega_{c,j}} C_j(\omega)v_j^2(\omega)\tau_j(\omega)d\omega \qquad (2.1)$$

where κ is the thermal conductivity, j is the phonon branch (e.g., acoustic or optical), $\omega_{\mathrm{c,j}}$ is the cutoff frequency, C_{j} is the volumetric heat capacity, v_{j} is the phonon group velocity, λ_{j} is the mean free path, ω is the angular frequency, and τ_{j} is the total

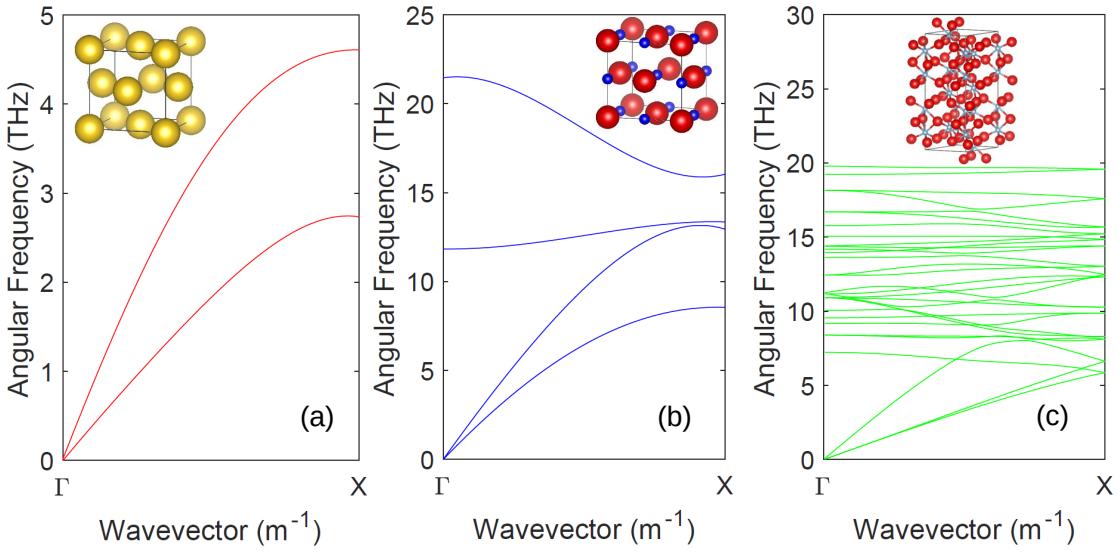

Figure 2.4: Phonon dispersion curves for (a) gold, (b) magnesium oxide, (c) sapphire; insets, crystal structures of each of the three materials. The dispersions are taken from Ref. [69] (gold), Ref. [70] (MgO), and Ref. [16] (sapphire). Crystal structures were created using VESTA software.[71, 72]

phonon scattering time that accounts for all possible phonon interactions. The heat capacity can be written as a function of the density of states, D_{j}, and distribution function, f:

$$C_j = \int_0^{\omega_{c,j}} \hbar\omega D_j(\omega) \frac{df}{dT} d\omega \tag{2.2}$$

For phonons, f is taken as the Bose-Einstein distribution function:

$$f = f_{BE} = \frac{1}{\exp(\frac{\hbar\omega}{k_B T}) - 1} \tag{2.3}$$

For isotropic crystals, a spherical Brillouin zone can be assumed, resulting in a phonon density of states given by

$$D_j(\omega) = \frac{\omega^2}{2\pi^2 v_j^3(\omega)} \tag{2.4}$$

Combining all of these expressions, the thermal conductivity can then be written as

$$\kappa = \frac{1}{3}\sum_{j}\int_{0}^{\omega_{c,j}} \frac{1}{2\pi^2 v_j(\omega)} \frac{\hbar^2\omega^4}{k_B T^2} \frac{\exp(\frac{\hbar\omega}{k_B T})}{(\exp(\frac{\hbar\omega}{k_B T})-1)^2} \tau_j(\omega) d\omega \tag{2.5}$$

In this equation, we integrate over ω, and many of the other variables are constants; this leaves only v_j and τ_j as unknowns. The group velocity can be determined from the phonon dispersion, since $v_\mathrm{j} = \partial\omega_\mathrm{j}/\partial\hbar$. To do this, it is often convenient to make a Debye approximation to simplify the analysis. In this approximation, the phonon modes are assumed to be non-dispersive and all of the phonons are assumed to have the same group velocity. This simplification agrees well with the real dispersion at the zone center, and so is a realistic approximation when low frequency phonons dominate thermal transport (i.e., low temperature relative to the Debye temperature of the material). However, the Debye approximation over-predicts the phonon frequencies near the edge of the Brillouin zone. There are several approaches that have been adopted to alleviate this high-phonon frequency failure of the Debye model. For example, the inclusion of a transition frequency where the real dispersion begins to deviate from the Debye approximation has been used;[73, 74] in this approach, after this frequency a second linear relationship with a lower group velocity can be assumed. In another approach to provide a more accurate analytical expression beyond a Debye dispersion, the phonon dispersion has been estimated from the analytical solution to vibrations of a one-dimensional atomic chain, which results in a sine-type relation.[75–78] While these various approximations can be adequate depending on the material system of interest, in general, it is ideal to obtain $\omega(\hbar)$ by fitting a higher order polynomial to the experimentally or computationally determined dispersion,[79] such as those shown in Figure 2.4. Once the group velocity has been determined, the only unknown is the total scattering time, which is related to the timescales of the

individual scattering processes via Matthiessen's rule,[1]

$$\tau_j^{-1} = \sum_i \tau_{i,j}^{-1} \tag{2.6}$$

where i indexes each specific scattering type in each branch j. We often use this term to model the thermal conductivity and determine the dominant scattering types.

One scattering mechanism involves interactions of phonons with other phonons in a system, often referred to as three-phonon scattering or Umklapp scattering, a term introduced by Peierls.[80] The rate at which phonon-phonon scattering occurs is dependent on both the phonon frequency and the temperature:[68, 81, 82]

$$\tau_{p-p}^{-1} = B\omega^2 T \exp(-\frac{C}{T}) \tag{2.7}$$

where B and C are material-dependent parameters that can be determined by performing a least squares fit on bulk thermal conductivity data.

The effect of phonons scattering at the sample boundary can also be considered. Taking d as the sample thickness, this term is given by

$$\tau_b^{-1} = \frac{v(\omega)}{d} \tag{2.8}$$

For bulk materials, d is relatively large, and so this term is negligible at high temperatures. In thin films, the phonon mean free path approaches the dimensions of the material, resulting in non-negligible phonon scattering at the film boundary.[68, 81–83]

The effect that these scattering terms have on modeling the thermal conductivity of a system is shown in Figure 2.5, in which the thermal conductivity is predicted as a function of temperature for magnesium oxide. As in other bulk materials, phonon-phonon scattering in bulk MgO results in a $1/T$ trend in the thermal conductivity at

higher temperatures. However, as the dimensions of the system are reduced, boundary scattering dominates and significantly reduces the thermal conductivity, as illustrated in Figure 2.5 for films of thicknesses ranging from 10 nm to 1 μm. As studied in

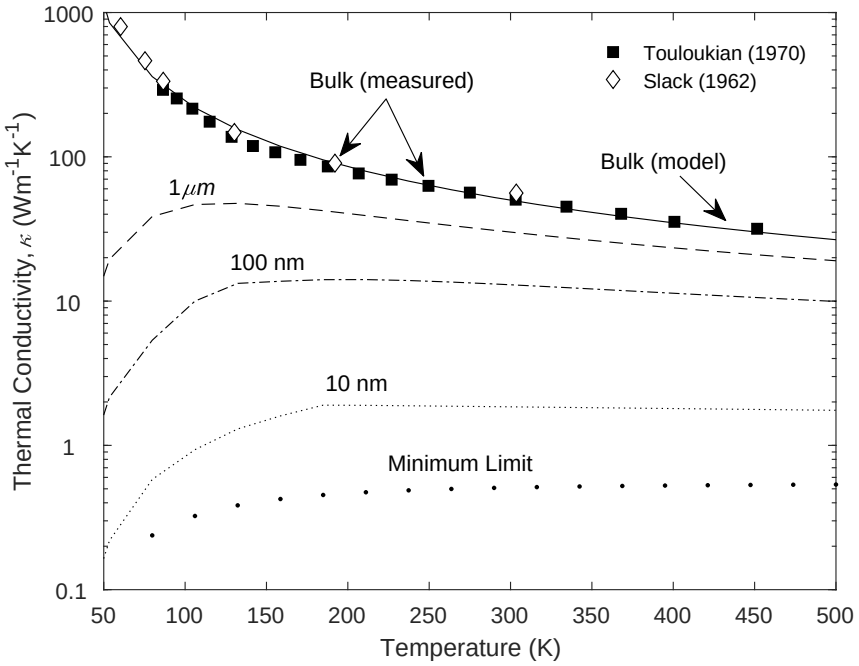

Figure 2.5: Models predicting the temperature-dependent thermal conductivity of magnesium oxide. The closed squares and open diamonds represent experimental bulk data from References [84] and [85], respectively, and models of thermal conductivity for bulk MgO (solid line), a 1 μm thick sample (dashed line), a 100 nm MgO thin film (dashed-dotted line), and the predicted minimum limit (dotted line), which is described in more detail below.

previous works,[86–90] phonons also scatter at grain boundaries. This term takes the form of

$$\tau_{gb}^{-1} = \frac{v(\omega)}{d_{grain}} \tag{2.9}$$

where d_{grain} is the average grain size. As with boundary scattering, phonon scattering with grain boundaries is dictated by the dimension of the crystal.

Impurities also play a role in scattering phonons, with a quartic dependence on

the phonon frequency:[91]

$$\tau_{imp}^{-1} = C\omega^4 \tag{2.10}$$

Point defect scattering has a similar frequency dependence, but with additional terms that account for perturbations due to changes in bond strength, mass, and atomic radius:[92, 93]

$$\tau_{def}^{-1} = \omega^4 x_{def} \left[\left(\frac{\Delta M_{def}}{M_{host}} \right)^2 + 2 \left[\left(\frac{\Delta G_{def}}{G_{host}} \right) - 6.4\gamma \left(\frac{\Delta \delta_{def}}{\delta_{host}} \right) \right]^2 \right] \tag{2.11}$$

where x_{def} is the concentration of defects, ΔM_{def} is the mass difference between the defect and the host atom compared to the mass of the host, M_{host}, G is the shear strength, and δ is the atomic radius. Phonon-vacancy scattering takes a very similar form, with the vacancy terms replacing those of defects:[94]

$$\tau_{def}^{-1} = \omega^4 x_{def} \left[\left(\frac{\Delta M_{vac}}{M_{host}} \right)^2 + 2 \left[\left(\frac{\Delta G_{vac}}{G_{host}} \right) - 6.4\gamma \left(\frac{\Delta \delta_{vac}}{\delta_{host}} \right) \right]^2 \right] \tag{2.12}$$

The defects discussed in the previous sub-section have also been theoretically and experimentally shown to scatter phonons.[68, 70, 95] For dislocations,

$$\tau_{dis}^{-1} = C_1 N_d |\mathbf{b}|^2 \omega \tag{2.13}$$

where C_1 is a constant related to the type of dislocation, N_{d} is the number of dislocations per unit area, and $\boldsymbol{b}$ is the Burger's vector. This scattering term is linearly proportional to the phonon frequency.

Knowledge of these scattering terms, in tandem with calculation of the heat capacity and group velocity (enabled by approximations to the dispersion), is the final component which enables us to fully capture the analytical model that describes thermal conductivity in phonon-dominated systems.

2.3 Thermal Transport in Amorphous Systems

In contrast to crystalline materials and as noted earlier, amorphous and glassy films lack atomic periodicity: while there can be local order, long-range order is non-existent. A phonon can only be defined if there exists a periodically repeating lattice. Instead, a different nomenclature is typically used to describe the modes of vibration in amorphous materials.[96] These modes can be described as either extended ("extendons") or localized ("locons"). Extendons can be further split into propagating ("propagons") and non-propagating ("diffusons") modes; locons are also non-propagating.[97] Of these various vibrational modes, propagons are most analogous to phonons in crystalline systems.

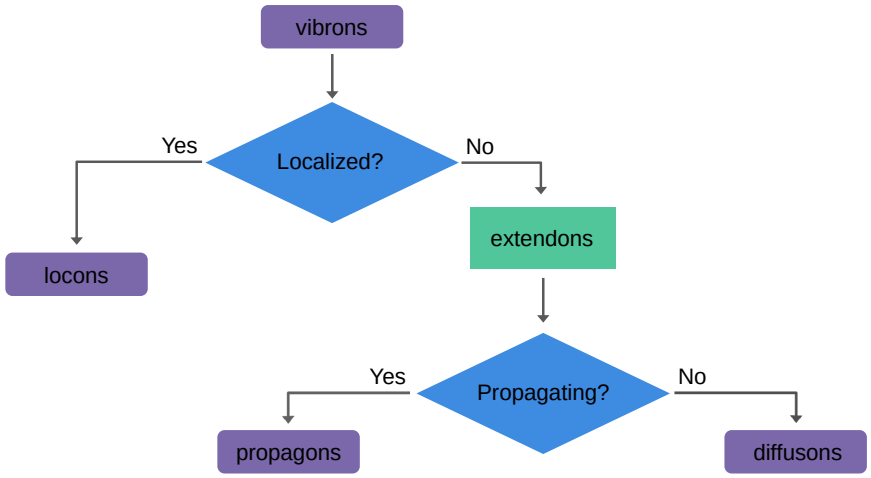

Figure 2.6: Taxonomy of vibrational modes in amorphous and glassy systems.

To put the thermal conductivity of low κ materials due to various phonon scattering mechanisms in context, experimental results are often compared to the minimum limit to thermal conductivity. Einstein originally proposed a thermal conductivity assuming that all phonon modes had the same vibrational frequency and estimating the mean free path to be on the order of the interatomic spacing.[61] Cahill and Pohl later refined this model by assuming a Debye distribution of phonons and estimating

the scattering time as half the period of oscillation of the atom.[98, 99] While this model does not generally predict the thermal conductivity of most materials, it does work well for many amorphous and disordered crystals. Assuming an isotropic solid, the minimum limit is given by[99]

$$\kappa_{min} = \frac{\hbar^2}{6\pi^2 k_B T^2} \sum_j \int_0^{\omega_{c,j}} \tau_{min,j} \frac{\omega^4}{v_j} \frac{\exp(\frac{\hbar\omega}{k_B T})}{\left(\exp(\frac{\hbar\omega}{k_B T}) - 1\right)^2} d\omega \tag{2.14}$$

where κ_{min} is the minimum thermal conductivity, j is the phonon polarization index, τ_{min} is the minimum scattering time, ω is the angular frequency, $\omega_{\text{c,j}}$ is the cut-off frequency, and v_{j} is the phonon group velocity. The minimum limit calculated for MgO is shown in Figure 2.5, and is shown to predict a thermal conductivity several orders of magnitude less than that of bulk.

2.4 Thermal Boundary Conductance

The thermal boundary conductance, also called the Kapitza conductance, relates the heat flux, q, to the temperature difference, ΔT, across a solid-solid interface:[100–102]

$$h_K = \frac{q}{\Delta T} \tag{2.15}$$

The thermal boundary conductance is an indication of how well an interface can conduct heat flow, which is related to the interfacial quality. Poor adhesion, roughness, and residue from the sample cleaning process can significantly reduce this boundary conductance.[103, 104] In a multilayer thermal model, the thermal conductivity and boundary conductance can be modeled by the concept of a thermal resistance circuit: the thermal resistances from each layer can be added in series to the resistance

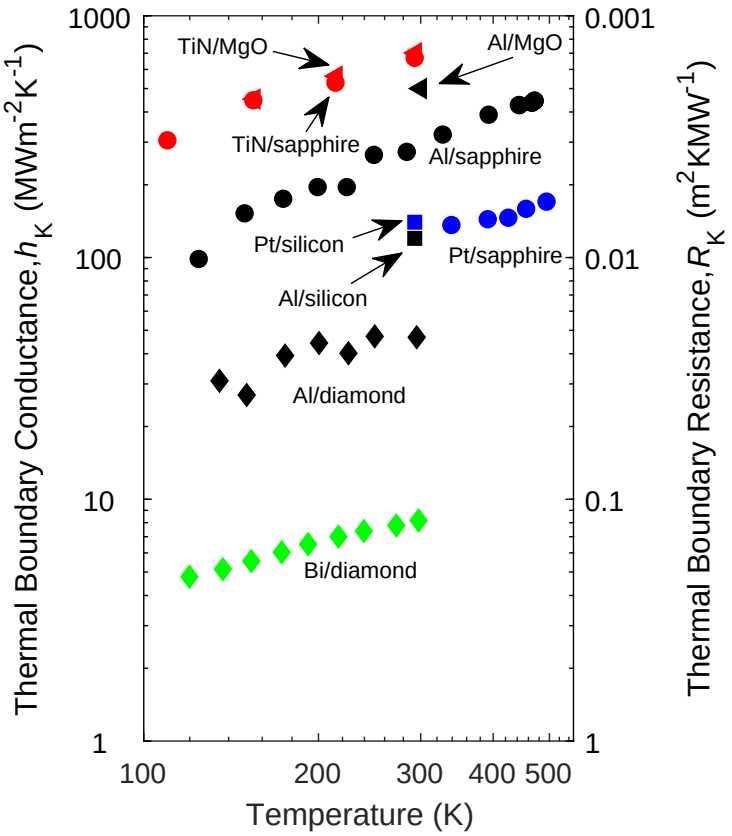

Figure 2.7: Representative temperature-dependent thermal boundary conductances for various metal/substrate interfaces. Data for h_K are taken from Ref. [105] (TiN/MgO and TiN/sapphire)), Ref. [106] (Al/MgO), Ref. [107] (Al/sapphire and Al/diamond), Ref. [108] (Al/sapphire and Pt/sapphire), Ref. [109] (Al/silicon and Pt/silicon), and Ref. [110] (Bi/diamond).

from the interface, $1/h_K$, as in

$$R_{total} = \frac{1}{h_{K,1}} + \frac{d}{\kappa} + \frac{1}{h_{K,2}} \tag{2.16}$$

Our experimental technique is most sensitive to the largest thermal resistance in this circuit. For example, a thin film of MgO between aluminum and sapphire will dominate the thermal resistance circuit because of its comparatively low thermal conductivity; in this case, an accurate measurement of the thermal boundary conductances could be difficult, and additional verification (such as a sensitivity analysis, discussed in more detail in Section 3.4) is necessary to confirm that the h_K's are resolvable. As

an additional example, a system comprising of a very thin (~2 nm) amorphous Al_2O_3 film (with $\kappa \sim 1$ $Wm^{-1}K^{-1}$) between aluminum and silicon will be dominated by the thermal boundary resistances: if the total interfacial resistance is estimated as ~200 $MWm^{-2}K^{-1}$ (a reasonable assumption), then the interfaces account for over 90% of the total thermal resistance. This means that our experiment is much more sensitive to the interfacial resistances and so, the thermal conductivity of the amorphous film cannot be isolated from the boundary resistances. In general, understanding the thermal boundary conductance is important because it can dominate thermal transport in some systems and impede accurate measurement of the thermal conductivity of films of interest.[111–113]

2.5 Summary

This chapter discussed disorder and defects in amorphous and crystalline materials and introduced the idea of phonons. In addition, the concepts of thermal conductivity and thermal boundary conductance were defined. The next chapter of this thesis discusses the experimental technique used to measure these thermal properties.

Chapter 3

Time-Domain Thermoreflectance

3.1 Experimental Background

Within our research group, the main experiment used to measure thermal conductivity (among other thermal properties) is time-domain thermoreflectance (TDTR), an optical pump-probe technique that utilizes sub-picosecond laser pulses to measure the change in reflectivity of a sample surface as a function of time after pump laser heating. Several references have detailed the principles and practices of TDTR in detail.[114, 115] TDTR relies on the principle of thermoreflectance to relate the change in reflectivity on the sample surface as a function of time after the pump heating event.[116–120] This is discussed in more detail in the next sub-section.

TDTR is attractive for a number of reasons: it is a non-contact, non-destructive characterization technique with a relatively high throughput. In addition, TDTR has the ability to monitor the temporal response to determine thermal properties over times ranging from picoseconds to nanoseconds, making this technique ideal for measuring the thermal properties of thin films. For example, a typical thermal diffusion time constant is ~100 ps for a 100 nm aluminum film and a characteristic interfacial time constant is ~900 ps for an interface between aluminum and sapphire;[121]

TDTR provides a unique method of investigating the underlying physical phenomena occurring during these extremely short timescales.

The TDTR systems used within this group were constructed by previous PhD students Dr. Ramez Cheaito and Dr. Brian Foley, and more detailed descriptions of these experiments and subsequent analysis are contained in their dissertations.[122, 123] A schematic of a TDTR experiment is shown in Figure 3.1. The TDTR used in the experimental work in this thesis is centered around a Ti:sapphire oscillator laser system that emits a train of laser pulses with a spectral width of ~11 nm (~100 fs) centered around 800 nm and a repetition rate of 80 MHz; the spectrum is monitored with an Ocean Optics spectrometer. The output of the oscillator passes through an optical isolator to prevent destabilizing reflections back into the laser cavity. This output is then energetically split into a pump and a probe beam using a polarizing beam splitter. The pump is modulated with an external electro-optic modulator (EOM)[124] to create a frequency-dependent temperature variation on the surface of the sample. The probe beam is delayed in time using a mechanical delay stage which controls the relative optical path length between the beams. After this time delay, the probe arrives at the sample surface and is focused collinearly with the pump. The cooling of the sample after pulse absorption, as monitored by the probe reflectivity, is measured by recording the in-phase (V_{in}) and out-of-phase (V_{out}) voltages from the lock-in amplifier as a function of pump-probe delay time. The reflection of the probe is monitored with a photodiode and contains a component at the pump modulation frequency. The back-reflection can be misaligned if the beam is not perfectly perpendicular to the sample surface; this can be rectified by making fine adjustments to the sample stage. Because the change in the thermoreflectance signal is on the order of $10^{-4}K^{-1}$,[125] a lock-in amplifier is necessary and enhances the signal to enable accurate measurements. Prior to measurements, the pump and probe beams are measured using a beam profiler (Thorlabs BP104-UV). Beam sizes vary

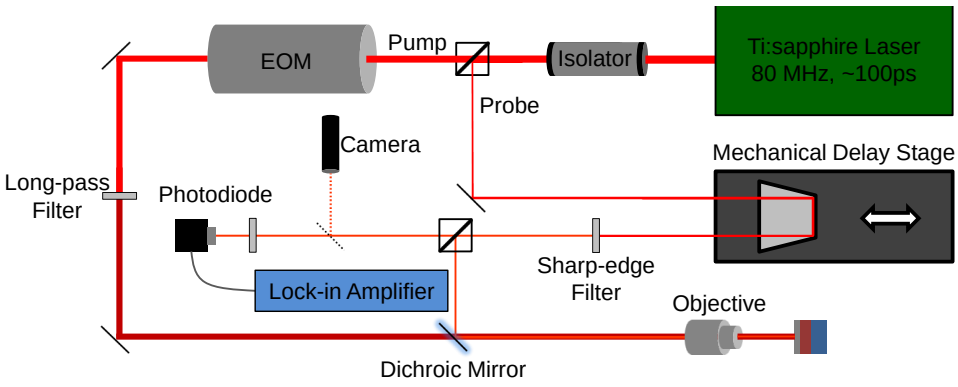

Figure 3.1: Diagram of TDTR; this schematic illustrates the two-tint configuration. The double color arrangement is slightly different: instead of using sharp filters to spectrally isolate the pump and probe, the pump is converted to 400 nm light after the EOM and a dichroic mirror reflects the pump onto the sample while transmitting the probe. Otherwise, the alignment procedures and detection mechanisms for both configurations are similar.

based on the magnification of the objective lens used; in this work, typical spot sizes were ~10-20 μm for the probe and 40-60 μm for the pump. In addition, a movable mirror can be used to steer the beams into a CCD camera, providing a convenient method for ensuring that the probe beam is focused on a smooth region of the sample surface.

In our lab, we have two main configurations for TDTR, double color and two-tint.[126] In the double color arrangement, the 800 nm (red) pump beam is converted to 400 nm (blue) light using a bismuth triborate (BiB_3O_6) crystal, a non-linear optical material which frequency doubles light using second harmonic generation,[127] while the probe beam remains at 800 nm. In the two tint setup, the pump and probe beams are spectrally separated off the laser spectrum using sharp edged filters. Both have benefits and disadvantages: while double color can provide more beam power, the bismuth triborate crystal can be prone to instabilities over time. The two tint arrangement, shown in Figure 3.1, is a lower power setup and thus, less suitable for measuring certain samples; however, the films measured in this work are not subject to this limitation. While I have measured the thermal properties of all of the samples

reported in this thesis on both systems, I performed the majority of testing on the two-tint TDTR experiment.

3.2 Thermoreflectance and pertinent thermal time scales after pulsed laser heating

As previously discussed, TDTR relies on the principle of thermoreflectance to relate the change in reflectivity on the sample surface as a function of time after the pump heating event. The analysis of my measurements requires that the probe beam reflectivity can be related to the temperature, and thus, the thermal properties of the sample of interest. The thermal model used to interpret TDTR data and measure the thermal boundary conductance across interfaces and thermal conductivity of the samples is reviewed extensively in the literature,[114, 122, 128–131] and thus not repeated here. Instead, the remainder of this chapter is devoted to various practices that I have implemented when analyzing TDTR data on thin films systems to accurately measure the thermal properties while properly accounting for statistical uncertainties and error.

While there have been studies investigating direct probing of samples,[132] typically samples to be measured with TDTR are coated with a thin (~80 nm) metal film. This ensures that the change in reflectivity of the sample surface is indicative of the change in temperature within the optical penetration depth of the metal film due to the ultrafast thermalization of electrons in a metal (near equilibrium temperature is established within a few picoseconds, allowing for the reflectivity to be directly related to temperature).[133, 134] From this, for small changes in temperature, ΔT, the change in reflectivity (ΔR) is given by

$$\Delta R = \frac{\partial R}{\partial T} \Delta T \tag{3.1}$$

and is driven by the thermal properties of the sample.

There are several pertinent time scales involved in laser heating, illustrated graphically in Fig. 3.2. In the first few picoseconds after the beam arrives at the sample surface, the pump pulse energy is absorbed by electrons in the metal transducer. These hot electrons thermalize and transfer their energy to the lattice, thereby increasing the lattice temperature. This early time scale is well suited to study non-equilibrium electron physics and electron-phonon coupling;[120,135–138] as previously mentioned, this regime lasts ~10 ps or so, and after this time regime, Eq. 3.1 can be implemented to relate the measured thermoreflectivity to parabolic-like single-fluid heat equations using pertinent symmetries and geometries to analyze the sample structure of interest.[114, 115, 128, 131, 133, 134] As the metal transducer is heated, a strain wave is generated due to the initial expansion of the lattice due to absorption of the pulse. If there is sufficient acoustic mismatch between the transducer and underlying material, part of this strain wave is reflected back at the interface and appears as an acoustic echo in the thermoreflectance scan.[139, 140] This effect is known as picosecond acoustics and can be used to understand interfacial quality[141–143] and determine the film thickness of the metal transducer.[144] After ~200 ps, sufficient heat has been diffused from the transducer to the film. In this regime, data can be fit to a multilayer thermal model that has been well described in the literature.[114,128,131,145] In this solution, there are multiple parameters associated with each layer; namely, heat capacity, thermal conductivity, film thickness, and the thermal boundary conductances across the various interfaces. Heat capacity is typically assumed from the literature and film thickness can be measured in a number of ways, including x-ray reflectivity, profilometry, ellipsometry, and the aforementioned picosecond acoustics. Generally, two parameters can be fit from a TDTR measurement; in this work, those variables are thermal conductivity and thermal boundary conductance. More details into the considerations necessary for these analyses are discussed below.

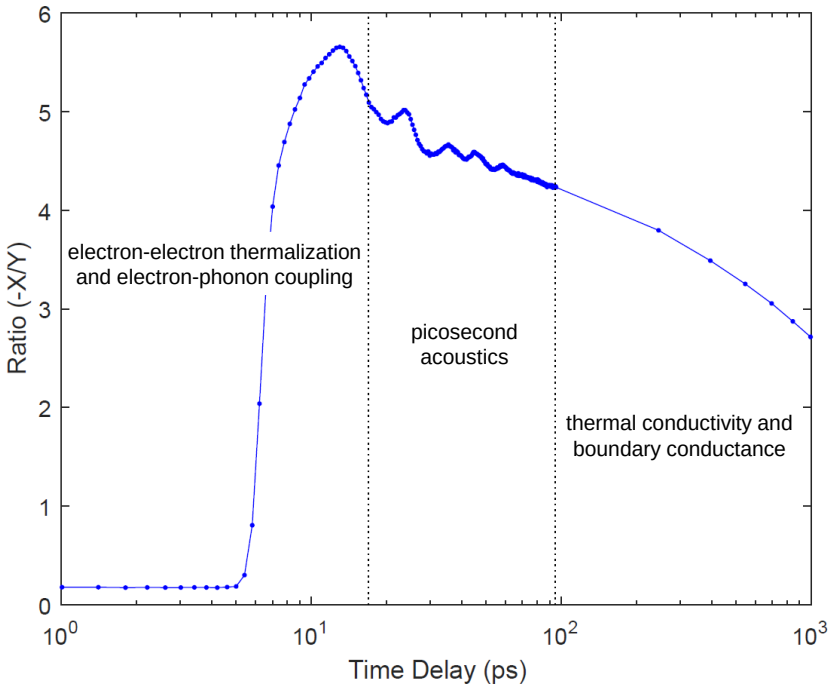

Figure 3.2: Typical TDTR data with highlighted pertinent time scales. This measurement was taken on a ~20 nm film of amorphous Al_2O_3 on quartz.

3.3 Calibration Measurements and Results

Testing calibrations prior to measuring other samples is a critical metric for gaging the robustness of the TDTR system: if a fit to data measured on the calibrations does not give the expected thermal conductivity, this is an indication of optics misalignment or another experimental issue. Typical calibration samples used prior to any measurement include sapphire, silicon, silicon dioxide, and fused quartz, which have been well characterized in the literature.[3, 4, 146–149] These materials span a large range of thermal conductivity values, from ~1.4 $Wm^{-1}K^{-1}$ (silicon dioxide) to ~140 $Wm^{-1}K^{-1}$ (silicon).[3, 4, 146] Representative TDTR data and fits for these calibration materials are shown in Fig. 3.3. The fitted thermal conductivities and thermal boundary conductances are tabulated in Table 3.1 and show good agreement with literature values. As a note, the thermal boundary conductance is not shown for silicon dioxide because TDTR is insensitive to h_K for low thermal conductivity materials, and so

Material	κ ($Wm^{-1}K^{-1}$)	h_K ($Wm^{-2}K^{-1}$)
Silicon dioxide	1.42 ± 0.1	-
Fused Quartz	11.48 ± 0.8	173 ± 8
Sapphire	35.74 ± 2.7	232 ± 18
Silicon	129.7 ± 9.5	243 ± 19

Table 3.1: Thermal conductivity, κ, and thermal boundary conductance, h_K, results for the calibration samples.

any fitted value of this interfacial conductance is not physical.

In a typical TDTR measurement, the temperature increase in the thin film due to the pump beam is on the order of a few degrees Kelvin and is negligible in the analysis.[128] However, for relatively low thermal conductivity materials, the temperature rise can be significant. The steady state temperature rise in the low frequency limit, ΔT, is given by[125, 128, 150]

$$\Delta T = \frac{P_0(1-R)}{2\sqrt{\pi}w\kappa} \tag{3.2}$$

where P_0 is the incident power, R is the reflectivity of the transducer film at the wavelength of the incoming beam, κ is the thermal conductivity of the material, and w is the beam radius. In low thermal conductivity materials, this effect can be minimized by reducing the powers used, but this is not always experimentally viable given that high enough beam powers are often necessary to induce a measurable signal. In these cases, we account for the additional heating in the analysis by modifying the value we assume for the heat capacities of the transducer and thin film of interest (since C is temperature dependent). This is especially critical when measuring SiO_2 and other low thermal conductivity materials, as failing to account for this temperature rise can give erroneous κ values that are 10-15% higher than the actual thermal conductivity, even when using relatively low pump and probe powers.

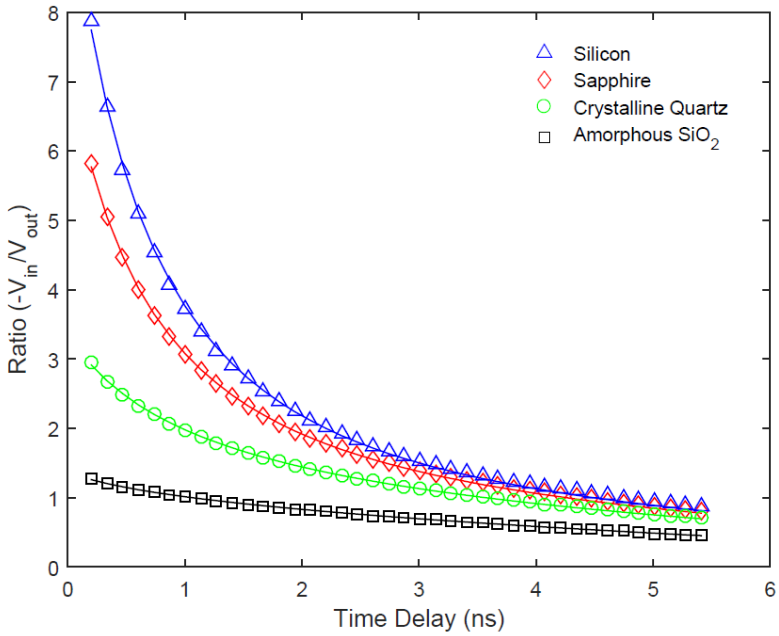

Figure 3.3: Representative TDTR data for typical calibration samples. The ratio of the in-phase to out-of-phase voltages is monitored and the data are fit to a thermal model. As seen here, the slope of the ratio of higher thermal conductivity materials (e.g., silicon) is much steeper than for lower κ materials (e.g., SiO_2).

3.4 Sensitivity Analysis

An important consideration in TDTR is the sensitivity of the measurement to the thermal properties of interest. In an ideal measurement, we are most sensitive to this parameter (e.g., thermal conductivity or thermal boundary conductance) and minimally sensitive to other experimental factors (e.g., transducer film thickness, beam spot sizes, and other thermal properties that are not of interest). This sensitivity is quantified using an approach described by Costescu et. al, where the sensitivity of a parameter of interest is related to the thermoreflectance signal through a logarithmic derivative.[105] The sensitivity factor is determined by

$$S_x = \frac{\partial \mathcal{S}}{\partial \ln(x)} \tag{3.3}$$

where S_x is the sensitivity, $\mathcal{S}$ is a component of the thermoreflectance signal (the in-phase or out-of-phase voltage or the ratio of the two), and x is the thermal property of interest. In general, the magnitude of the sensitivity indicates how confidently we can determine that parameter. Additionally, a significant difference in the curvature of any two parameters allows fitting for both parameters simultaneously: if the curvatures are similar, then these two parameters cannot be isolated from one another in the analysis.

Example sensitivity analyses of the ratio to the thermal conductivity and thermal boundary conductance for the calibration samples (sapphire, silicon, fused quartz, and silicon dioxide) are shown in Fig. 3.4. For silicon and sapphire, the magnitude of the sensitivities of κ and h_K is non-zero and the curvatures are relatively steep, indicating that we can confidently fit for and distinguish between both parameters. However, for lower thermal conductivity materials, such as silicon dioxide, this is not the case: while the magnitude of the sensitivity to κ is non-zero, the magnitude of h_K is near zero and the curvature is nearly flat over the time regimes of interest, indicating little or no sensitivity to the boundary conductance. As discussed earlier, typically, the ratio of the in-phase to out-of-phase voltages from the lock-in amplifier is analyzed to determine the thermal conductivity and thermal boundary conductances across the interfaces. However, in certain cases, TDTR measurements are also sensitive to the back-side conductance (film/substrate); in this case, the ratio alone cannot be used to determine the thermal conductivity of the thin film because it cannot be adequately resolved from the boundary conductances. Instead, the front-side conductance is determined using only the in-phase signal; with this information, the thermal conductivity of the film and back-side conductance is fitted with the ratio.

This sensitivity analysis is also important when selecting a modulation frequency,

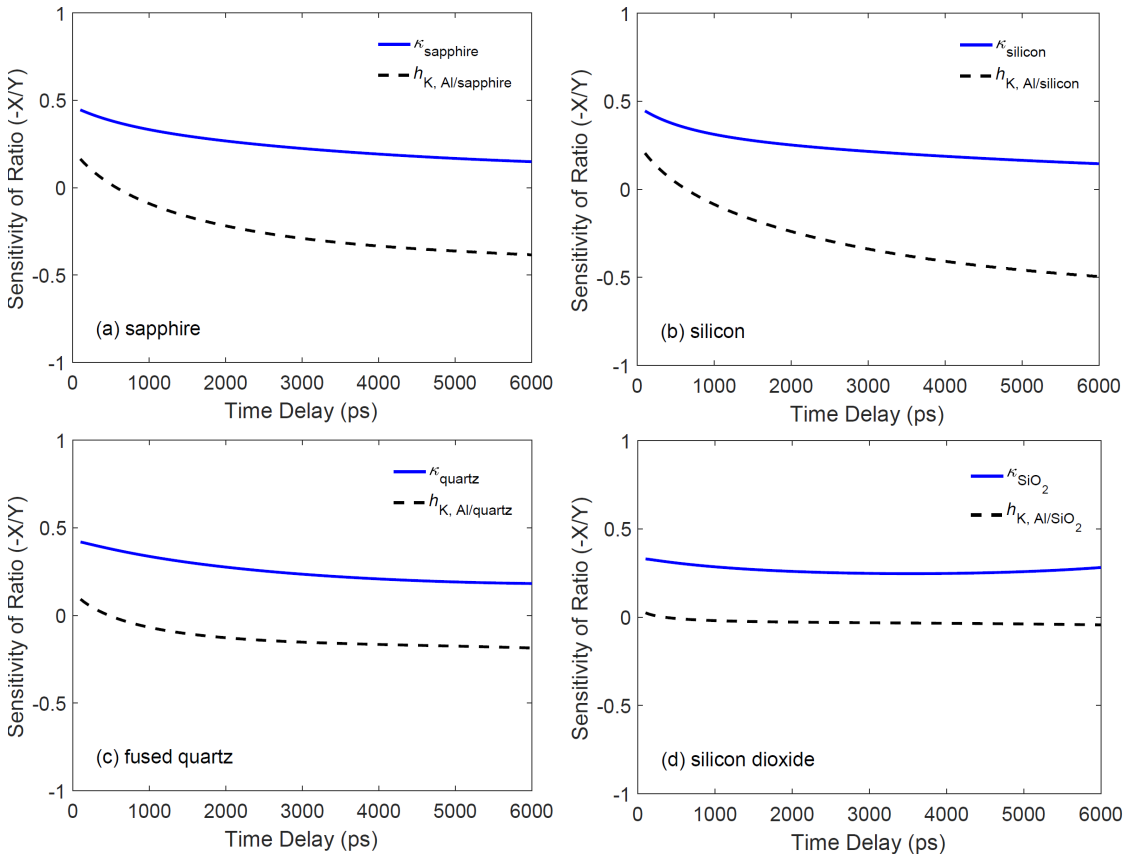

Figure 3.4: Sensitivities of the thermal conductivity (blue/solid line) and thermal boundary conductance (black/dashed line) between a 80 nm aluminum transducer and (a) sapphire; (b) silicon; (c) fused quartz; and (d) silicon dioxide.

which is related to the thermal penetration depth by[151]

$$L_z = \sqrt{\frac{\kappa}{\pi f C}} \tag{3.4}$$

where L_z is the thermal penetration depth, κ is the thermal conductivity, f is the pump modulation frequency, and C is the volumetric heat capacity. At high frequencies, the penetration depth is shallow compared to the pump radius, resulting in one-dimensionally dominated thermal diffusion in the cross-plane direction. At low frequencies, the thermal penetration can become comparable to the pump radius and in-plane heat diffusion must also be considered, which complicates the analysis. Comparing the sensitivity of the cross- and in-plane thermal conductivity as a function of

spot size and modulation frequency justifies the assumption of one-dimensional heat transfer.[151] All of the work presented in this thesis used relatively high modulation frequencies (~3-10 MHz) to constrain thermal diffusion in the cross-plane direction.

3.5 Sources of Error

The most significant source of error in TDTR is the film thickness of the metal transducer. This thickness can be verified with x-ray reflectivity, profilometry, and picosecond acoustics with an accuracy of ±3 nm for an 80 nm thick film. We account for this uncertainty by perturbing the transducer thickness by ±3 nm in the analysis and calculating the resulting changes in thermal conductivity and thermal boundary conductance, $\Delta\kappa_{\mathrm{d}}$ (for κ). We also consider the variations in data taken across the sample surface. In this work, at least 6-8 measurements were made on each sample and the standard deviation was determined, $\Delta\kappa_{\mathrm{data}}$. The total error is then taken as the square root of the sum of the squares of each source of uncertainty, given by

$$\Delta\kappa_{total} = \sqrt{{\Delta\kappa_{data}}^2 + {\Delta\kappa_d}^2} \tag{3.5}$$

In addition, the samples discussed in this study were measured on both the double color and two tint systems, providing an additional metric by which to compare the experimental data. Within the calculated uncertainties, there was no difference in the results from the two systems. The slight variations in the measurements on each system were accounted for in the reported uncertainties.

3.6 Summary

This chapter introduced time-domain thermoreflectance, including the basic principles behind the technique and important experimental considerations. Measure-

ments of calibration samples were provided as an example of representative TDTR data. A typical sensitivity analysis is presented and general sources of error are discussed.

Chapter 4

Phonon-Defect Scattering in MgO Thin Films

4.1 Introduction

Defect-induced deviations in lattice structure can give rise to phonon scattering processes and changes in the phonon thermal conductivity of crystals. Where ample experimental works have studied and validated classical scattering theories regarding phonon-grain boundary and phonon-impurity thermal resistances on bulk- and nano-scales,[68,78,81,86,87,95,152,153] the phonon scattering mechanisms contributing to thermal resistances at finer scale defects, such a small angle tilt boundaries and dislocations, have been much less frequently studied.[95] This has led to voids in the depth of understanding of the interplay between, and importance of, phonon-lattice defect scattering relative to the interaction of phonons with other static impurities, such as incoherent grain boundaries, mass impurities, and interfaces between dissimilar materials. Progress in this fundamental understanding of the phonon-lattice defect interaction will have major impacts in the design of novel classes of material systems, such as the recently discovered systems synthesized by utilizing screw dislocations,[154–158]

high figure of merit thermoelectric materials designed with dense dislocations arrays,[158] nanostructures with dislocation dense interfaces that impact the thermal boundary conductance,[103, 159, 160] and thermal transport in ferroelectric materials where coherent ferroelastic domain walls affect the phononic resistance.[161–163]

Here, we report on measurements of the room temperature thermal conductivity of a series of magnesium oxide (MgO) nanocrystalline thin films in which the crystalline coherence lengths (the characteristic length of crystal devoid of translational symmetry-breaking defects) of the MgO films are varied. Small angle tilt boundaries defining crystallites of similar dimensions to the measured crystal coherence length were previously identified in identically processed films. In addition to grain boundaries and other crystallographic defects, such as dislocations, these were attributed to a damping of optical phonons.[58] It is therefore anticipated that these same defects may affect the transport of heat-carrying phonons. We use time domain thermoreflectance (TDTR)[128] to measure the thermal properties of the MgO thin films at room temperature and atmospheric conditions; by utilizing a combination of both the in-phase and the ratio of the in-phase to out-of-phase components of the TDTR response in tandem, we demonstrate the ability to measure the thermal conductivity of the MgO films at a single modulation frequency, while separating the influence of thermal boundary conductance across both the front and back thin film interfaces from this thin film thermal conductivity measurement. We show that the thermal conductivities of the MgO films increase with an increase in crystalline coherence length, which is correlated with not only the defects that limit the crystalline coherence, but also is indicative of a changing average lattice parameter of the MgO. Our work demonstrates the ability to quantify the influence of defects on the phonon thermal conductivity by an average length scale of crystal translational symmetry – the crystalline coherence length. Our results suggest that this crystalline coherence length scale provides a measure of the limiting phonon mean free path in crystalline

solids, a quantity that can be determined via standard X-ray reflectivity and is often difficult to measure and observe with traditional microscopy techniques.

4.2 Experimental Details

4.2.1 Sample Fabrication

The 80 nm thick MgO film series was prepared on (100)-oriented silicon substrates via 30° off-axis RF magnetron sputter deposition within a Kurt J. Lesker Lab 18 instrument. Prior to loading in the load-locked sputter chamber, the substrates underwent a 7:1 buffered HF etch (pH of 5.5) and de-ionized-H_2O rinse to remove the native silicon dioxide surface. The film was sputtered from a single-phase sintered MgO target in 5 mTorr of argon at room temperature with a power density of 3.7 W/cm^2. The wafer was subsequently divided and sections were processed between 200°C and 800°C in 200°C intervals in air for one hour; varying the annealing temperature directly correlates to a change in crystalline coherence length.[58] Silicon was chosen as a substrate due to its predicted phase stability and chemical inertness with MgO in this temperature range, suggesting the formation of clean interfaces with no secondary phases during the deposition and annealing process;[164] furthermore, the high thermal conductivity of silicon ensures maximum sensitivity to the thermal conductivity of the MgO thin films in our TDTR measurements.

4.2.2 Structural Characterization

Phase purity and crystalline coherence lengths were characterized via X-ray diffraction (XRD) using a Philips X'Pert MPD with Cu Kα radiation in the Bragg-Brentano geometry. As such, the diffraction vector is normal to the sample surface and the only lattice planes to which we are collecting diffracted X-rays are those that are parallel to the film surface (actually, parallel to the (001) planes of silicon, to which the

instrument was aligned, but for all intents and purposes is parallel to the surface). Therefore, crystallite dimensions to which this technique is sensitive are those normal to the film surface – the same direction as thermal conductivity is measured. Crystalline coherence lengths were calculated using X-ray line broadening and Scherrer's formula.[165] All XRD measurements were conducted by Dr. Jon Ihlefeld and Dr. Elizabeth Paisley at Sandia National Laboratories.

The surface roughnesses, thicknesses, and density of the annealed samples were characterized using a combination of atomic force microscopy (AFM), X-ray reflectivity (XRR) and variable-angle spectroscopy ellipsometry (VASE) by collaborators at North Carolina State University, Dr. J.-P. Maria and Dr. Christopher Shelton. Cross-sectional and plan-view microstructural images (Fig. 4.1(a-f)) were obtained by scanning electron microscopy with an FEI Verios. Secondary electron images were collected with an electron landing energy of 500 V and 2000 V stage bias. Average grain sizes were determined from the plan-view images using the linear intercept method.[166] Additionally, 78 nm thick aluminum films were electron-beam evaporated onto the samples for use as transducers in subsequent TDTR scans. The precise aluminum film thicknesses were determined using both mechanical profilometry and picosecond acoustic measurements during subsequent TDTR scans.[139, 140]

As shown in the SEM images in Fig. 4.1(a-f), polycrystalline grains with columnar morphology comprise the films. Figure 1g shows the coherent scattering lengths of X-rays for the MgO samples processed between room temperature and 800°C, and reveals a trend of increasing length with post-deposition processing temperature, similar to that reported previously in identically processed MgO thin films.[58] Scattering lengths were calculated using the (200) MgO X-ray reflection; the measured coherence lengths varied from 5.4 nm for the as-deposited sample to 19.5 nm for the 800°C processed sample. Lattice parameters were also determined from (200) peak position using the silicon (400) reflection as a reference for sample displacement error

correction. Shown in Fig. 4.1(h), the lattice parameter is reduced with increasing coherence length. The data indicate that the higher the degree of crystalline perfection, the more closely the lattice parameter approaches the accepted single crystal value of 4.21 Å.[167] In these fine crystallite size films, it is likely that disorder near surfaces, defects, and grain boundaries gives rise to these expanded lattice parameters, as has been suggested previously for fine-grained MgO.[168] SEM images of the sample series shown in Fig. 4.1(a-f) indicate that physical grain size, as defined by the distance between well-defined grain boundaries, is constant among the sample series, where the average grain size is 20.9 ± 1.3 nm, indicating that the varying crystalline coherence length is not driven by grains separated by large angle boundaries. Additionally, no obvious change in density or porosity was observed with annealing condition. No statistically significant variation in film thickness was identified (average of measurements from XRR and VASE, and listed in Table 4.1), further suggesting that film density was constant among the sample series. However, increasing the annealing temperature did lead to changes in the MgO surface roughnesses and the formation of increasingly thick SiO_2 layers between the MgO and silicon substrate with increased temperature. More specifically, the MgO surface roughness increased from 2.8 ± 1.2 nm for as-sputtered samples to 9.3 ± 5.3 nm for the sample annealed at 800°C (average of measurements from XRR, VASE and AFM, and listed in Table 4.1); also, we detected an increasingly thick SiO_2 layer between the MgO and silicon that grew to as thick as 6.1 ± 1.2 nm after the 800°C anneal (average of measurements from XRR and VASE, and listed in Table 4.1). We note that the relatively large uncertainties in our reported average values for SiO_2 thicknesses could be indicative of the different sensitives of XRR and VASE to this buried SiO_2 film, as the uncertainties are determined from the standard deviation among the data collected with each technique. Regardless, the temperature dependent variations in our samples were confined around the top and bottom MgO film interfaces. Therefore, since the microstructural properties

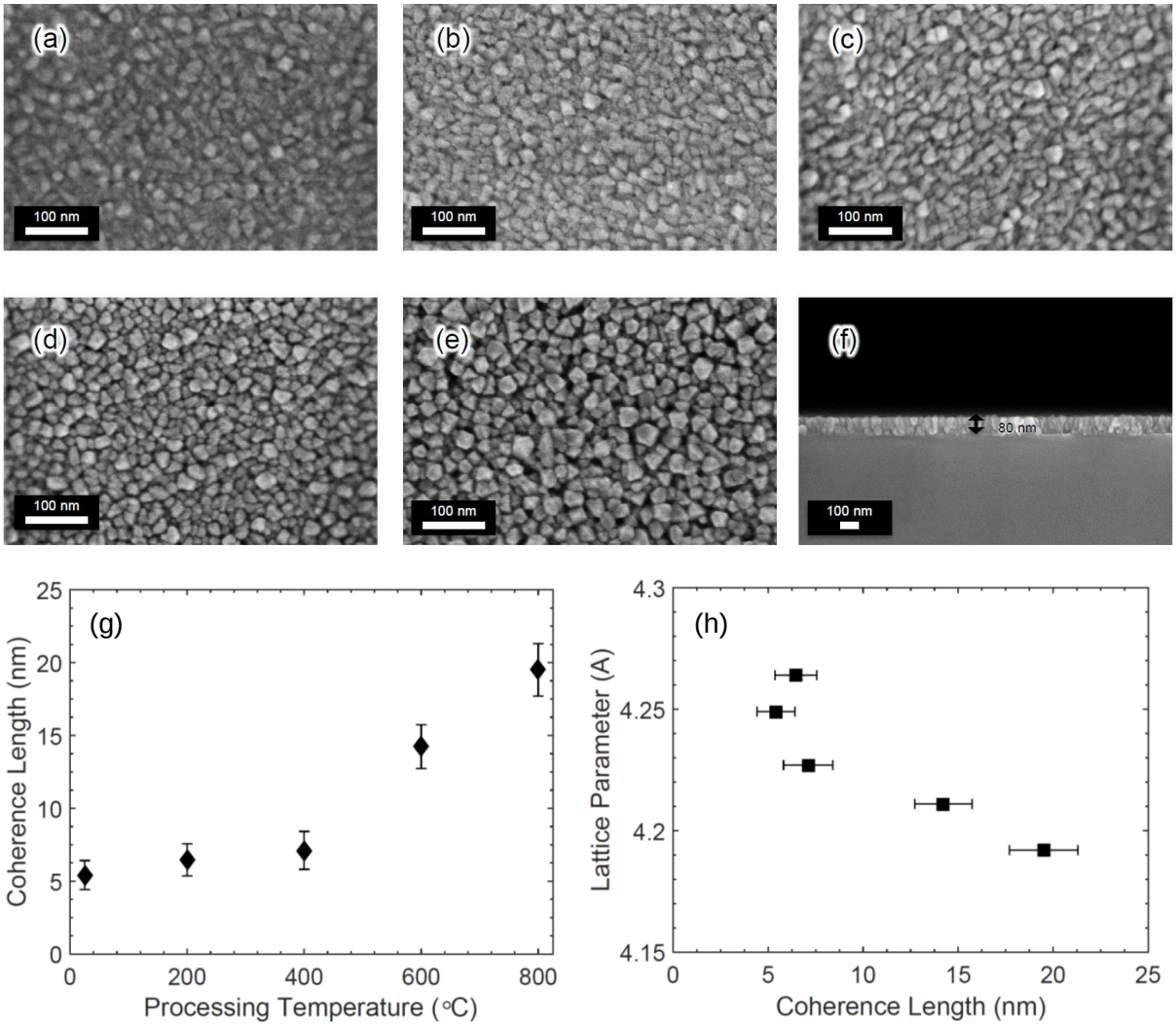

Figure 4.1: SEM images for varying processing temperatures: (a) 25°C, (b) 200°C, (c) 400°C, (d) 600°C, (e) 800°C; (f) cross-section for representative sample; (g) coherence length as a function of temperature; (h) lattice parameter as a function of coherence length. The SEM plan view images show that grain size and porosity are consistent among all of the films, and the cross-sectional images show that all films are 80 nm thick. The coherence length is found to vary in direct proportion to the processing temperature. As the crystallinity increases, the measured lattice parameter decreases and approaches the single crystal value intrinsic to MgO.

Anneal Temperature (°C)	MgO film thickness (nm)	MgO surface roughness (nm)	SiO_2 layer roughness (nm)
N/A	84.0 ± 2.8	2.8 ± 1.1	native
200	78.9 ± 4.9	5.8 ± 3.4	3.8 ± 3.8
400	79.3 ± 3.5	4.7 ± 1.8	3.4 ± 3.1
600	83.6 ± 1.7	5.1 ± 2.3	3.5 ± 2.1
800	82.4 ± 1.6	9.3 ± 5.3	6.1 ± 1.2

Table 4.1: MgO film thickness (average of measurements made with XRR and VASE), MgO surface roughness (average of measurements made with XRR, VASE and AFM), and thickness of SiO_2 layer between MgO and Si substrate (average of measurements made with XRR and VASE). The uncertainty reported in these measurements represent the standard deviation among all the values determined from the different techniques.

in the MgO films away from the film boundaries are comparable among all of the films, this suggests that the only factor varying within the bulk of the film is the crystalline coherence length, which has previously been verified.[58]

4.2.3 Thermal Measurements

The thermal conductivities of the MgO films were determined using TDTR by fitting the data to a multi-layer thermal model described in detail in the literature.[114,118,128,131] Briefly, TDTR is a non-contact optical pump-probe technique that uses a short-pulsed laser to both produce and monitor modulated heating events on the surface of a sample. The laser output from a sub-picosecond oscillator is separated into pump and probe paths, in which the relative optical path lengths are adjusted with a mechanical delay stage. The pump path is modulated to create a frequency dependent temperature variation on the surface of the sample, and the in-phase and out-of-phase signals of the probe beam locked into the modulation frequency of the pump were monitored with a lock-in amplifier. Prior to TDTR measurements, the sample surfaces were coated with a thin aluminum film so that the changes in reflectivity of the surfaces were indications of the change in tempera-

ture within the optical penetration depth of the aluminum; this change in reflectivity is driven by the thermal properties of the MgO film, the silicon substrate, and the thermal boundary conductances across the Al/MgO and MgO/Si interfaces. We assume literature values for the heat capacities of the aluminum,[169] MgO,[170] and silicon,[84] leaving the unknowns in our thermal models as the thermal boundary conductances across the Al/MgO and MgO/Si interfaces ($h_{\mathrm{K,\ Al/MgO}}$ and $h_{\mathrm{K,\ MgO/Si}}$, respectively) and the thermal conductivity of the MgO film, κ_{MgO}.[114]

Typical TDTR analyses on thick films or substrates can analyze the ratio of the in-phase to out-of-phase signals from the lock-in amplifier to determine the thermal conductivity and thermal boundary conductance across the metal/sample interface (assuming a relatively high thermal effusivity). However, in the case of our MgO thin films, our TDTR measurements are also sensitive to the thermal boundary conductance across the MgO/Si interface, even at relatively high modulation frequencies (~10 MHz). Therefore, we cannot use the ratio signal alone to measure the thermal conductivity of the MgO since we cannot uniquely separate this from the two thermal boundary conductances. To overcome this experimental limitation, we modify our analysis approach by utilizing a combination of both the in-phase signal and the ratio of the in-phase to out-of-phase components of the TDTR response in tandem. The in-phase component of the lock-in frequency response is sensitive to the Al/MgO interface during the first nanosecond of a TDTR scan, since the in-phase component is related to the single pulse response in the time domain, as shown in Fig. 4.2(a). Exploiting this sensitivity, we fit the data for the front-side boundary conductance using the real component, then apply this value when using the ratio to fit for both the back-side conductance and MgO thermal conductivity. As shown in Fig. 4.2(b), the ratio is highly sensitive to the thermal conductivity of the MgO and the thermal boundary conductance at the MgO/Si interface. While the ratio is only marginally sensitive to the thermal boundary conductance across the Al/MgO interface, this

sensitivity can vary based on the thermal conductivity of the MgO, which changes by a factor of ~3 among the films studied in this work. Therefore, this approach is necessary to accurately measure the thermal conductivity of the MgO, while also evaluating the corresponding uncertainty in our measurements. We discuss this approach in more detail, including sensitivity analyses in our previous work.[171]

Using this aforementioned analysis approach in an interactive fashion, we measure $h_{\mathrm{K,\ Al/MgO}}$, $h_{\mathrm{K,\ MgO/Si}}$, and κ_{MgO} at a single TDTR scan at a single frequency. To ensure accuracy of this approach, we measure $h_{\mathrm{K,\ Al/MgO}}$, $h_{\mathrm{K,\ MgO/Si}}$, and κ_{MgO} at different pump modulation frequencies. Our measured results of the thermal conductivities and thermal boundary conductances are shown in Fig. 4.3(a) and (b), respectively, for two representative samples (those with the largest and smallest coherence lengths: 800°C annealed and as-deposited samples, respectively). We measured $h_{\mathrm{K,\ MgO/Si}}$ to be relatively constant across all the samples (~200 – 300 $\mathrm{MWm^{-2}K^{-1}}$), indicating the negligible influence of the change in SiO_2 thickness at the MgO/Si boundary on $h_{\mathrm{K,\ MgO/Si}}$. We find no statistically significant and appreciable change in the thermal conductivity or boundary conductances with varying frequency, indicating the robust ability of our approach to measure the intrinsic thermal conductivity of thin films with a single TDTR measurement at one modulation frequency when thermal boundary conductance could influence the thermal response. This elucidates a unique analysis procedure when using TDTR to measure the thermal properties of thin films. Our reported uncertainties in the values reported for thermal conductivities and thermal boundary conductances are determined by considering three different sources of error. First, we calculate the standard deviation among the entire set of measurements for each sample (multiple measurements on each sample). Second, we assume a ~10% uncertainty in the Al transducer film thickness. Finally, we determine a 95% confidence interval for each measurement. We take the square root of the sum of the squares of each deviation from the mean values resulting from these sources of uncertainties to

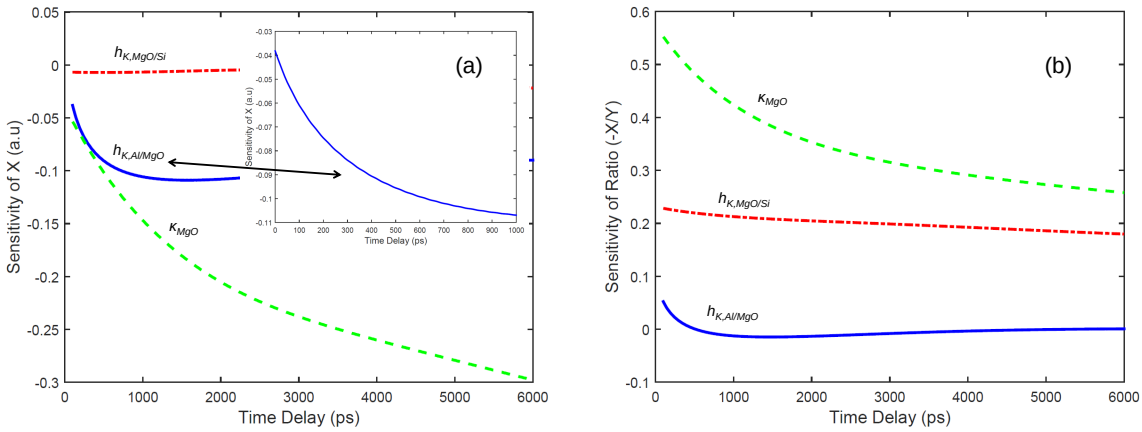

Figure 4.2: Sensitivities of our thermal model for determining the thermal boundary conductances across the Al/MgO and MgO/Si interfaces ($h_{\mathrm{K,\ Al/MgO}}$ and $h_{\mathrm{K,\ MgO/Si}}$, respectively) and the thermal conductivity of the MgO (κ_{MgO}) from analyzing the (a) in-phase and (b) ratio of in-phase to out-of-phase TDTR data.

construct our error bars. We note that largest uncertainties in our reported values lie in the samples with the highest thermal boundary conductances and highest thermal conductivities. This is consistent with the fact that as the thermal conductivity of the MgO thin films increase (or the interfaces conductances increase), and hence, the corresponding thermal resistances decrease, our TDTR measurements become less sensitive to these thermophysical properties. However, our reported values still lie within a 95% confidence bound. Along these lines, it is worth noting that the apparent observed frequency dependence in the thermal conductivity measurements of the MgO samples with the maximum coherence length (Fig. 4.3(a)) are nearly constant when considering our aforementioned confidence interval, and still only deviate ~20% about the mean; in other words, this fluctuation in our measured data for thermal conductivity with frequency is not physical, but just an artifact of the sensitivity of TDTR for measuring relatively thermally conductive thin films (i.e., films with relatively low thermal resistance), especially when using lower pump modulation frequencies where the thermal penetration depth is increased and therefore sampling more of the underlying substrate relative to the thin film. However, as the coherence

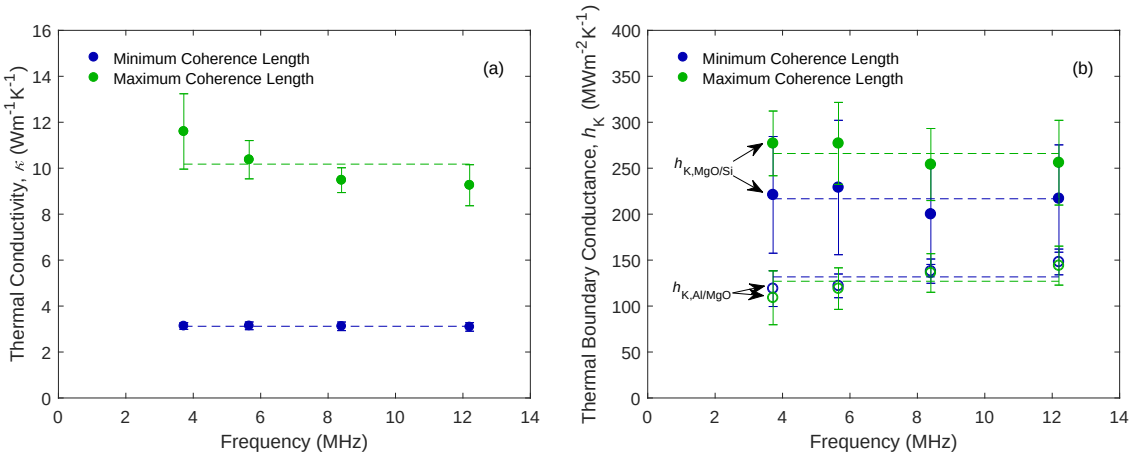

Figure 4.3: (a) Thermal conductivities and (b) thermal boundary conductances as a function of modulation frequency. Analyzing the in-phase signal in tandem with the ratio of the in-phase to out-of-phase signal, we find that, within a standard deviation, the thermal conductivities and thermal boundary conductances for the maximum and minimum coherence lengths are constant among varying modulation frequencies. This is confirmation that our analysis technique enables us to determine $h_{\mathrm{K,\ Al/MgO}}$, $h_{\mathrm{K,\ MgO/Si}}$, and κ_{MgO} from a single TDTR scan at any given modulation frequency.

length in the MgO thin film is decreased, and the thermal conductivity is lowered, TDTR measurements are much more robust and sensitive in measuring thermal conductivity, consistent with the relatively minor uncertainty associated with our fits.

4.3 Results and Discussion

Measuring the thermal conductivity as a function of crystallinity, we find that thermal conductivity varies with the coherence length and plateaus as the crystalline coherence length approaches the average grain size (20.9 $\pm$ 1.3 nm), as depicted in Fig. 4.4. The thermal conductivity begins to plateau at larger crystalline coherence lengths because the coherence length of these samples are ultimately limited by the large angle grain boundaries. This is consistent with Matthiessen's rule, which asserts that the shortest phonon scattering length scale will dominate the average mean free

path. Therefore, the large reduction in the measured thermal conductivities of these MgO samples compared to bulk single crystalline MgO (Ref. [172]) are due to the grain boundaries for the largest coherence lengths and limited by various imperfections in the crystal as the coherence length is decreased. Because the film thickness, density, grain size, and porosity are consistent among the sample series, the only factor that changes in these polycrystalline films is the crystalline coherence length, further supporting this observation of a transition from imperfection-limited thermal conductivity at small coherence lengths to grain boundary limited thermal conductivity at the larger coherence lengths. We note that the surfaces of the MgO film are changing

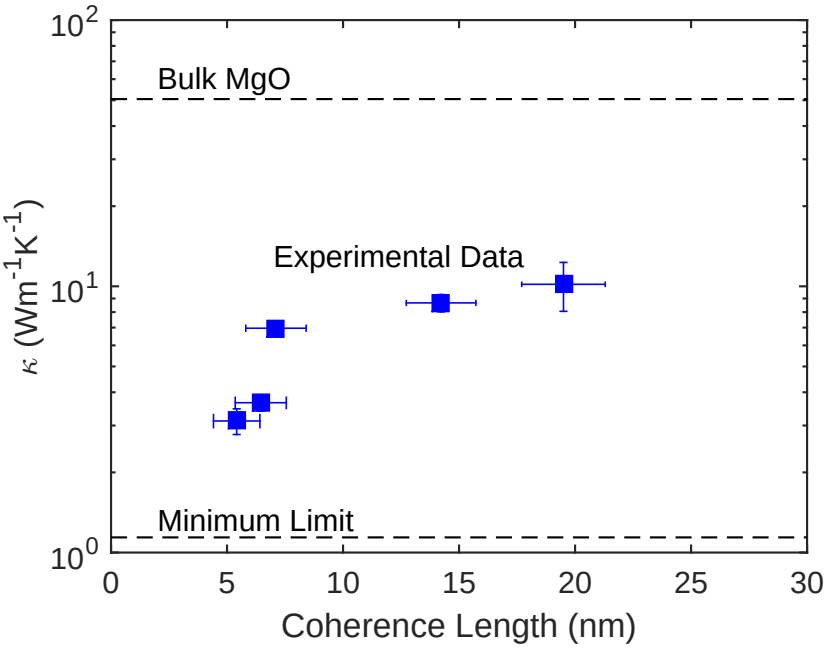

Figure 4.4: Thermal conductivity as a function of coherence length. The bulk value for MgO given from Touloukian et al. is shown for comparison.[172] We observe an increase in thermal conductivity with increasing crystalline coherence length, which is ultimately limited by the grain size of the polycrystalline MgO films. The reduction in crystalline coherence length leads to MgO samples with thermal conductivities that are roughly a factor of 4 higher than the predicted minimum limit (Eq. 4.1), a factor of 3 lower than the largest coherence length sample (limited by grain boundary scattering, which remains constant for all coherence lengths), and a factor of 10 lower than bulk MgO.[172]

among the samples processed at different temperatures; as previously mentioned, with increasing MgO processing temperature, the MgO surface becomes more rough and the SiO_2 layer between the MgO and silicon becomes thicker. However, we measure an increasing thermal conductivity with increased temperature, which would imply that the increased surface roughness and increase in SiO_2 thickness, which would add thermal resistance to the system, play only a minor role in our thermal conductivity measurements of MgO compared to the changing crystalline coherence length. This also gives further support to our data representing the intrinsic thermal conductivity of the MgO, and our ability to separate the resistances at the MgO interfaces from our reported values of κ_{MgO}.

To put the magnitude of the reduction in thermal conductivity due to the crystalline coherence length scales into perspective, we turn to the minimum limit to thermal conductivity.[99] Assuming an isotropic solid, the minimum limit is given by

$$\kappa_{min} = \frac{\hbar^2}{6\pi^2 k_B T^2} \sum_j \int_0^{\omega_{c,j}} \tau_{min,j} \frac{\omega^4}{v_j} \frac{\exp(\frac{\hbar\omega}{k_B T})}{\left(\exp(\frac{\hbar\omega}{k_B T}) - 1\right)^2} d\omega \tag{4.1}$$

where κ_{min} is the minimum thermal conductivity, j is the phonon polarization index, τ_{min} is the minimum scattering time, ω is the angular frequency, $\omega_{\mathrm{c,j}}$ is the cut-off frequency, and v_{j} is the phonon group velocity. To evaluate Eq. 4.1 for this material system, we use a Debye assumption with sound velocities of the acoustic branches taken from the experimentally determined dispersion[70] in the [100] direction. While the lowest thermal conductivity sample is a factor of 4 higher than the thermal conductivity predicted from the minimum limit, it is lower than the bulk thermal conductivity by an order of magnitude.[172]

To confirm that this variation in thermal conductivity is due to the change in crystalline coherence length, and not merely a result of changing lattice parameter, we compare our experimental results to the Leibfried-Schlomann equation[173, 174]

given by

$$\kappa = \frac{\beta M a \theta_D^3}{T\gamma^2} \tag{4.2}$$

where β is a factor inversely related to γ (the Gruneisen parameter), M is the average atomic mass, a is the lattice constant, θ_{D} is the Debye temperature, T is temperature, and γ is the Gruneisen parameter[175] given by

$$\gamma^2 = \frac{a^6}{\omega^2}\left(\frac{\partial\omega}{\partial(a^3)}\right)^2 \tag{4.3}$$

We determine $\partial\omega/\partial(a^3)$ from the experimentally measured transverse optical frequencies, which depend on unit cell volume[58] and scale the Debye temperature for each film assuming $\theta_{\mathrm{D,\ film}} = \theta_{\mathrm{D,\ lit}}(a_{\mathrm{film}}/a_{\mathrm{lit}})$. Through this analysis, we observe opposite trends when comparing our experimental results to the predicted variation of thermal conductivity due to lattice spacing. This implies that the change in lattice parameter among the sample series is not responsible for the variation in thermal conductivity, rather, that defects responsible for the crystalline coherence are the driving force impacting phonon scattering.

This demonstrates the ability to quantify the influence of defects on the phonon thermal conductivity the crystalline coherence length of the crystal. This has the advantage of offering limiting length scales for phonon transport in crystalline system in which imperfections are difficult to characterize and/or model. For example, using molecular dynamics simulations, Ni et al.[95] showed that localized strain field, varying atomic spacing, and modifications to the intrinsic anharmonic phonon-phonon interaction strength near defects, such as dislocation cores, must be accounted for to properly model the phonon-lattice defect dynamics in the thermal conductivity. Unlike phonon-grain boundary and phonon-mass impurity-limited thermal transport,[68,78,81,86,87,95,152,153] modeling these processes is not easily or accurately feasible with simplified kinetic theory-type models, and therefore predictions of

changes in thermal conductivity due to these imperfections can be daunting. However, our work suggests that the characterization of a crystalline coherence length gives insight to qualitatively compare changes in thermal conductivity of similar materials with different degrees of crystalline imperfections.

As a final note, our experimental measurements in Fig. 4.3(b) show a relatively negligible dependence of thermal boundary conductance with crystalline coherence length of the MgO. We have previously observed that interfacial imperfections can lead to changes in thermal boundary conductance.[103, 141] Given that we do not observe any substantial structural changes at the surfaces of the MgO films, we would not expect any changes in thermal boundary conductance, which is consistent with our measurements of h_K at each interface. Furthermore, it interesting to note that the Al/MgO thermal boundary conductance is consistently lower than the MgO/Si thermal boundary conductance regardless of the MgO crystalline coherence length. While more work must be done that specifically focuses on the role of interface defects, our results highlight the potential impact of our previously discussed TDTR analysis to extract the thermal boundary conductance across thin films interfaces, and using this to assess the role of changes in atomic-scale defects at material interfaces on changes (or lack thereof) in thermal boundary conductance.

4.4 Summary

In conclusion, we have investigated the effects of crystallinity changes on thermal conductivity of MgO thin films. We find a systematic increase in thermal conductivity with increasing coherence length. Our thermal model, while sufficient for many other material systems and phonon scattering processes, fails to account for this crystallinity effect. This is consistent with previous studies, and implies that much more complex modeling is necessary to understand the effects of dislocations on phonon scattering.

Chapter 5

Density and Size Effects in Amorphous Al_2O_3 and TiO_2 Thin Films

5.1 Introduction

Amorphous oxide thin films are ubiquitous in microelectronics and nanotechnologies, including use as dielectric and passivation layers in transistors,[46, 176] light absorption layers in thin-film photovoltaics,[177] and chemically stable thermal isolation layers in biological and electronic devices.[13, 178] Common techniques for depositing these amorphous oxide thin films include ion beam, RF, and DC sputtering,[179–182] vacuum and reactive evaporation,[180, 181, 183] wet chemical processes,[180] and chemical vapor deposition (CVD).[184–186] While all of these deposition processes produce "amorphous" films, their mechanical[187] and transport properties,[188, 189] including thermal conductivity, can vary considerably based on differences in film density, impurity level, and short-range order.

Atomic layer deposition (ALD) is a chemical vapor deposition technique based

on self-terminating, surface-limited gas-solid reactions.[44, 190–193] ALD is unique among thin film deposition techniques because it can conformally coat complex three-dimensional structures, precisely control film growth rate at sub-nanometer length-scales, and systematically vary the atomic density of amorphous films.[194] ALD's intricate control over growth rates and atomic density of amorphous oxide films provides an opportunity to customize the electronic, optical, and thermal properties of these materials. Here we investigate how the thermal conductivity of ALD grown amorphous TiO_2 and Al_2O_3 films depends upon atomic density and thickness.

While the thermal conductivity of inorganic, non-metallic amorphous thin films has been the subject of a considerable number of experimental studies over the past several decades,[147,176,179,181,195–213] there has been much less attention paid to the thermal conductivity of amorphous films grown by ALD-techniques, specifically targeting the role that deposition conditions can have on the resulting thermal conductivity of the material.[102,191,214–218] In our previous work,[214] we have shown the strong dependence that the chamber temperature during ALD-growth can have on the thermal conductivity of ~50 nm thick Al_2O_3 thin films via the atomic density of the film varying by as much as ~15% (resulting in a ~35% change in thermal conductivity). Clearly, this strong influence of growth temperature on atomic density and thermal conductivity can also propagate additional thermal transport considerations when varying the thickness, thereby introducing vibration-interface scattering and subsequent thermal boundary resistances at the thin film boundaries. Given the potential of precisely grown ALD thin films in a wide array of technologies, the interplay between atomic density and film thickness on the thermal conductivity of thin films must be better understood.

ALD's precision in controlling film thickness and density also affords the opportunity to systematically test the validity of various predictive models that have been proposed for the thermal conductivity of amorphous systems. For example, many

amorphous systems are proposed to follow the minimum limit model for thermal conductivity.[61, 99, 219, 220] The minimum limit model only requires a knowledge of the speed of sound and atomic density of the solid and has demonstrated good agreement with many amorphous and other disordered systems with low thermal conductivities.[221] However, for heterogeneous materials that have undergone changes to their local atomic structure or a reduction in atomic density, this model fails to adequately capture observed trends in thermal conductivity.[208, 214] Modifications to this minimum limit model have been proposed to try and account for these deficiencies.[206, 214]

Our current work is thus motivated by these aforementioned voids in the understanding of both thermal properties of ALD-grown films and density effects on thermal conductivity in amorphous systems. In this work, we study the role of deposition conditions that vary density and film thickness on the thermal conductivity of amorphous ALD grown TiO_2 and Al_2O_3 thin films. By varying the temperature during the ALD growth, the atomic density of the deposited film is controlled, as evident by the changing optical properties. We measure the thermal conductivities of the films with varying densities and film thicknesses with time-domain thermoreflectance (TDTR). In general, we find that the thermal conductivity of these material systems is significantly reduced by decreasing atomic density. Furthermore, we find that size effects do not significantly impact the intrinsic thermal conductivity at relatively small thicknesses, which has been shown in other amorphous thin films.[214, 222, 223] However, the overall resistance of the amorphous films and adjacent interfaces becomes dominated by the influence of the thermal boundary resistances as the film thickness is reduced, as expected for purely diffusive thermal transport.

In addition to providing advances in the physics of thermal transport in amorphous structures and establishing metrics for ALD-grown thin films, our study further advances the understanding of ALD-growth and thermal transport in the specific ma-

terial systems studied in this work. In particular, amorphous alumina (a-Al_2O_3) and titania (a-TiO_2) are thermal insulators that are of interest to a wide array of the technologies discussed above, since they can be deposited at low temperatures,[13,14] are biologically stable,[13] and chemically inert.[13–18] In addition, a-TiO_2 has been studied for use as an optical coating and in sub-wavelength optical structures due to its relatively high refractive index.[14,41–45] The refractive indices of a-Al_2O_3 and a-TiO_2 have been well studied and found to correlate with atomic density[214,224,225] like other amorphous films.[145,206,221,226,227] This work provides clear relationships among growth conditions, refractive index, and thermal conductivity for these materials that will greatly aid in the development of material systems, technologies and devices that rely on a-Al_2O_3 and a-TiO_2.

5.2 Experimental Details

5.2.1 Atomic layer deposition for thin film growth

All of the samples studied in this work were fabricated by Dr. Mark Losego and Brandon Piercy at the Georgia Institute of Technology.

Thin films of a-Al_2O_3 and a-TiO_2 were deposited using a homebuilt hot-wall, flow-tube ALD reactor controlled by a custom LabVIEW sequencing program. Trimethylaluminum (TMA) and titanium tetrachloride ($TiCl_4$) were used as-received (Strem, 99%) as the metal precursors for Al_2O_3 and TiO_2, respectively, with deionized water as the oxidant. Ultra-high purity nitrogen (Airgas, 99.999%) was used as a carrier gas. Silicon substrates (WRS, test grade) were air plasma-cleaned before deposition.

Depositions were conducted by repetitive sequencing of metal precursors (t_1) and oxidant (t_3) doses separated by purge steps (t_2, t_4) in the order $t_1/t_2/t_3/t_4$ (all times given in seconds). For Al_2O_3 depositions a 0.1/30/0.1/30 deposition sequence was used to achieve a deposition rate of approximately 0.11 nm/cycle at all process tem-

peratures (50 and 200°C). For a-TiO_2, two deposition processes were used in order to calibrate the a-TiO_2 growth rate at low temperatures. Initially, a sequence of 0.5/45/0.1/30 was used for 1000 cycles across the temperature range (38-100°C), depositing films from 104-67 nm thick. Subsequently, films with target thicknesses of 50 nm were deposited at 38, 50, 75, and 100°C, and films with target thicknesses of 10, 20, 30, and 40 nm were deposited at 50 and 100°C. In this second series, different purge durations were used to maintain characteristic ALD deposition rates between 0.05 and 0.07 nm/cycle such that above 100°C, the sequence used was 0.5/45/0.1/30 while below 100°C the sequence used was 0.5/90/0.1/45. All film thicknesses and refractive indexes were measured with spectroscopic ellipsometry (alpha-SE, J.A. Woollam Co.) and fit using a Cauchy model.

5.2.2 Time-domain Thermoreflectance

To determine the thermal conductivity of our samples, we used time-domain thermoreflectance (TDTR). TDTR and details of the corresponding analyses are described elsewhere.[114, 128, 131] Briefly, TDTR is a non-contact, non-destructive optical pump-probe technique that takes the output of a 80 MHz, 100 fs Ti:Sapph. oscillator and energetically splits it into pump and probe paths. The pump beam instigates a modulated heating event on the surface of the sample via an external modulator (electro-optic modulator - EOM), while the probe is delayed in time using a mechanical delay stage. After being delayed in time, the probe beam arrives at the sample surface, is focused collinearly with the pump, and the probe's reflection is then monitored with photodiode directed to a lock-in amplifier that is triggered to the frequency of the EOM (the pump beam heating event). In this work, we modulate the pump path between 3.72 and 12.2 MHz. We monitor the in-phase (V_{in}) and out-of-phase (V_{out}) voltages recorded from the lock-in amplifier as a function of pump-probe delay time, and analyze the ratio of these voltages ($-V_{\text{in}}/V_{\text{out}}$) to deter-

mine the thermal conductivities of the films. Due to various optical components in our experimental layout, the pulse width of the pump and probe is stretched by the time it reaches the sample surface, yielding a cross-correlation of ~700 fs. However, the thermal conductivity of the amorphous film is determined over pump-probe delay times of 100's of picoseconds to nanoseconds, therefore, the precise pulse widths of the sub-picosecond pulse is irrelevant.

The thermal conductivities of these amorphous thin films were determined using a multi-layer thermal model fit to the ratio of the in-phase to out-of-phase voltages, as described in the literature.[114, 131, 145] We assume literature values[84, 169] for the heat capacities of each of the layers, and then scale the heat capacities of the amorphous films proportionally to their reduced atomic densities. Additionally, we determine the thermal conductivities of the substrates by measuring control samples of silicon and quartz; these measured values are consistent with the literature.[172] For our thickest films (~50 nm), we are able to analyze our data using a three layer model and directly measure the thermal conductivity. However, the thinner films (~10-40 nm for TiO_2 and ~2-20 nm for Al_2O_3) are thin enough that they are in a regime where the film thermal conductivity cannot be isolated from the front-side and back-side interfacial resistances, $R_{\mathrm{Al}/a\text{-film}}$ and $R_{a\text{-film/substrate}}$, respectively.[151] Therefore we determine an effective thermal conductivity, which contains both the intrinsic thermal conductivity of the amorphous thin film and the boundary resistances. The implications of this are discussed in the following section. We determine the uncertainty in our measurements by considering two different sources. First, we calculate the standard deviation among the entire set of measurements for each sample. Second, we determine the change in thermal conductivity due to perturbing the aluminum transducer thickness by ±3 nm in our analysis. From this, we construct our error bars by taking the square root of the sum of the squares of each source of uncertainty.

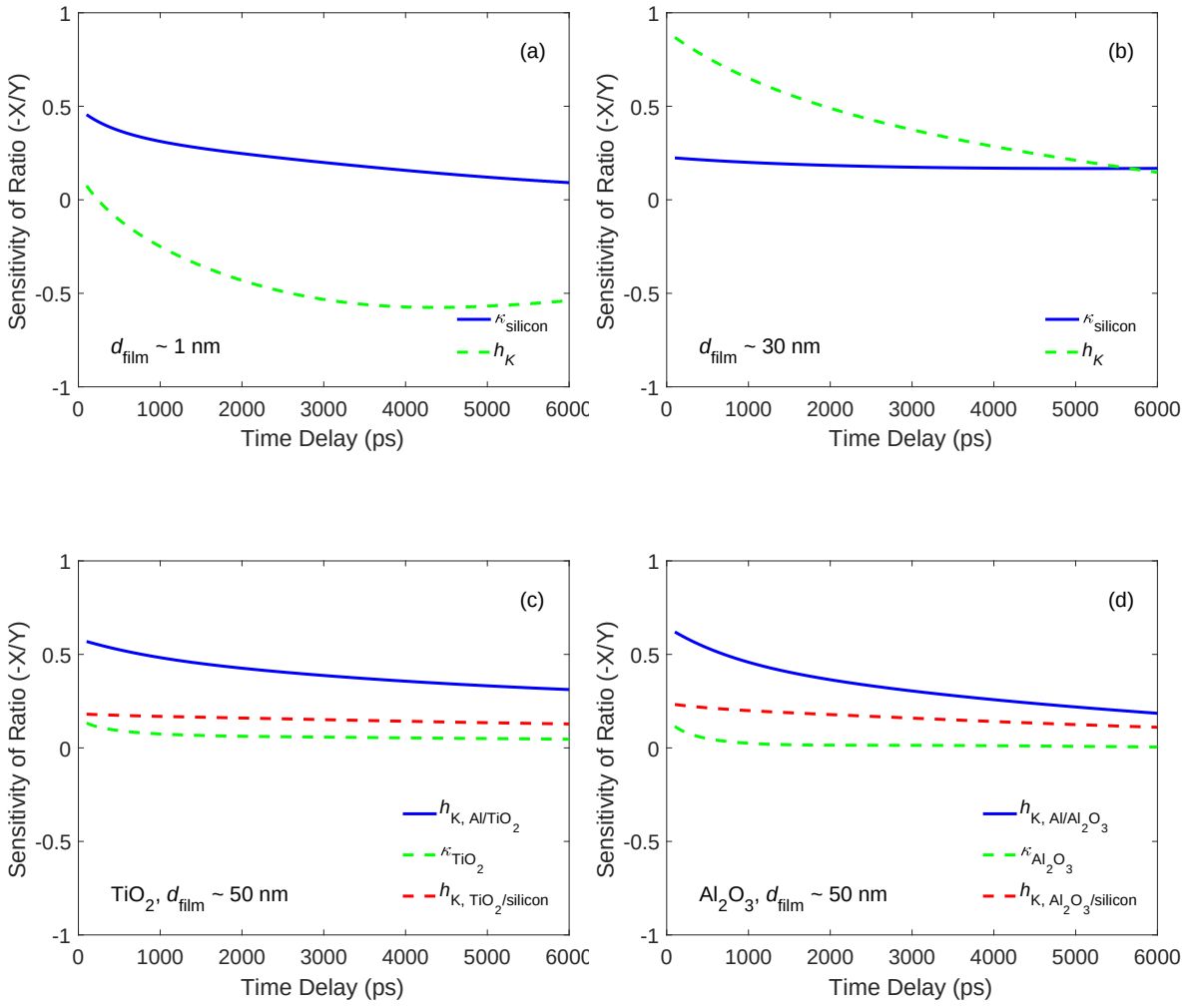

Figure 5.1: Sensitivity analyses of amorphous Al_2O_3 and TiO_2 thin films for (a) a two layer model for the thinnest films (~1 nm); (b) a two layer model for thicker films (~30 nm); (c) a three layer model for ~50 nm *a*-TiO_2 on silicon; (d) a three layer model for ~50 nm *a*-Al_2O_3 on silicon.

5.3 Results and Discussion

5.3.1 Thickness Dependence

The measured thermal resistances, R, and calculated effective thermal conductivities, κ_{eff} for the a-Al_2O_3 and a-TiO_2 films are shown in Fig. 5.2. The effective thermal conductivity is determined as $\kappa_{\text{eff}} = d/R$,[228] where d is the film thickness. The a-Al_2O_3 films were deposited onto both silicon and quartz substrates, and the measured thermal resistances of the a-Al_2O_3 films do not depend on the substrate. This suggests that the thermal resistance that dominates these TDTR measurements is not substrate dependent. Additionally, we observe a systematic increase in R (and hence κ_{eff}) as a function of film thickness, which is consistent with previous studies on the thermal properties of amorphous thin films. This has been attributed to the increased influence of the thermal boundary resistances on the overall measured thermal resistance as the film thickness decreases.[176, 222, 223, 228, 229] To gain more insight into the relative roles of the intrinsic thermal conductivity of the thin films and the influence of thermal boundary resistances on our TDTR measurements, we fit our measured data to a series-resistor model, as described previously[176]. Here the effective thermal conductivity is approximated by

$$\kappa_{eff} = \frac{\kappa_i}{1 + \frac{R_{tot}\kappa_i}{d}} \tag{5.1}$$

where R_{tot} is the total thermal boundary resistance from both interfaces (Al/film and film/substrate) and κ_{i} is the intrinsic thermal conductivity. Representative model fits of Eq. 5.1 to the effective thermal conductivity data are shown in Fig. 5.2 (b) and (d) for the a-TiO_2 and a-Al_2O_3 films, respectively. From these fits, we determine a thickness independent thermal conductivity of the amorphous films, the results of which are presented in Tables 5.1 and 5.2. Furthermore, we estimate the thermal

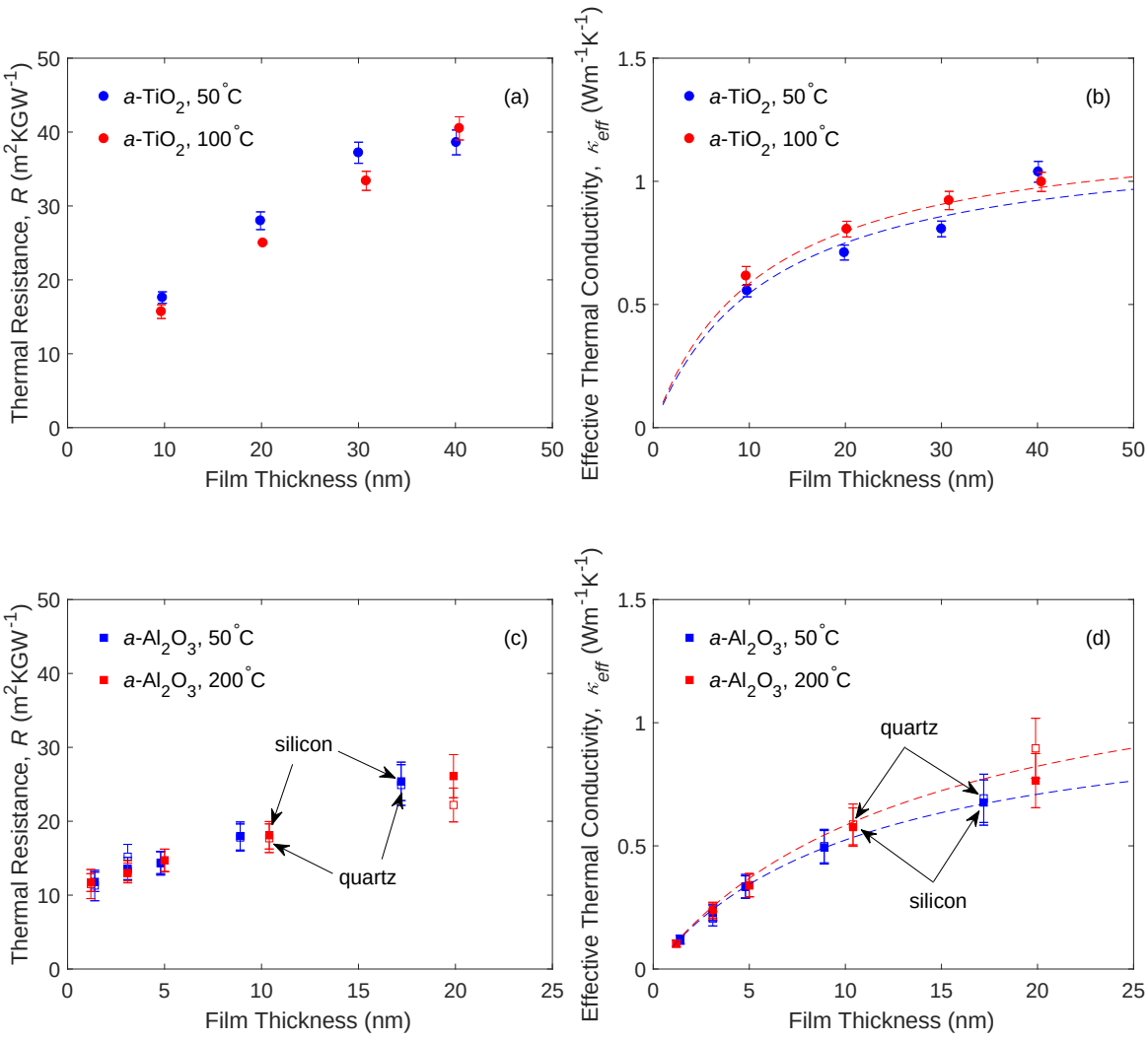

Figure 5.2: Measured thermal resistance, R, and calculated effective thermal conductivity, $\kappa_{\text{eff}} = d/R$, of these amorphous thin films. (a) and (b) show R and κ_{eff} for a-TiO_2 and (c) and (d) show R and κ_{eff} for a-Al_2O_3. The Al_2O_3 films were deposited onto both silicon and quartz substrates, which are indicated in each plot as open and closed circles, respectively. The dashed lines are fits to a series-resistor model, from which we can determine an intrinsic thermal conductivity that is thickness independent.

Deposition Temperature (°C)	Amorphous film thickness (nm)	Index of Refraction	Atomic densities (10^{28}m^{-3})	a-TiO_2 κ (W m^{-1} K^{-1})
38	50.8 ± 0.02	2.34 ± 0.05	6.92	1.20 ± 0.09
	104.0 ± 0.02	2.35 ± 0.05	6.99	1.15 ± 0.08
50	≤ 40	2.38 ± 0.01	7.18	1.2 ± 0.1
	50.6 ± 0.1	2.38 ± 0.04	7.18	1.26 ± 0.08
	93.1 ± 0.02	2.41 ± 0.05	7.37	1.26 ± 0.09
75	50.1 ± 0.03	2.43 ± 0.05	7.50	1.47 ± 0.12
	78.7 ± 0.01	2.46 ± 0.03	7.70	1.42 ± 0.1
100	≤ 40	2.48 ± 0.02	7.83	1.3 ± 0.1
	48.1 ± 0.1	2.47 ± 0.05	7.76	1.49 ± 0.13
	67.8 ± 0.01	2.49 ± 0.04	7.89	1.48 ± 0.11

Table 5.1: Amorphous TiO_2 film thickness, growth temperature, refractive index, calculated atomic densities, and measured thermal conductivity. The thermal conductivities for the films ≤ 40 nm were determined from a series resistor model fit to multiple samples of varying thicknesses (c.f., Fig. 5.2).

Deposition Temperature (°C)	Amorphous film thickness (nm)	Index of Refraction	Atomic densities (10^{28}m^{-3})	a-Al_2O_3 κ (W m^{-1} K^{-1})
50	≤ 20	1.60 ± 0.05	8.02	1.1 ± 0.1
	50.6 ± 0.03	1.60 ± 0.05	8.02	1.05 ± 0.09
200	≤ 20	1.66 ± 0.05	9.29	1.6 ± 0.2
	59.7 ± 0.04	1.66 ± 0.05	9.29	1.63 ± 0.12

Table 5.2: Amorphous Al_2O_3 film thickness, growth temperature, refractive index, calculated atomic densities, and measured thermal conductivity. The thermal conductivities for the films ≤ 40 nm were determined from a series resistor model fit to multiple samples of varying thicknesses (c.f., Fig. 5.2).

boundary resistances (conductances) as ~10 m^2KGW^{-1} (~100 ± 10 $MWm^{-2}K^{-1}$) for all sample sets, regardless of material, substrate, or deposition temperature. This is reasonable given previous works which measured the thermal boundary conductance across metal/non-metal interfaces,[104,109,230] however, we are relatively insensitive to this boundary conductance due to the high thermal resistance from the amorphous thin films. This is consistent with previous studies measuring similar materials.[176, 179] In addition, the lack of substrate dependence on R or κ_{eff} indicates that the thermal resistance most likely originates from the metal/film interface and not from the interface between the film and the substrate.

5.3.2 Density Effects

Figure 5.3 shows the measured thermal conductivity of the a-Al_2O_3 and a-TiO_2 films due to the change in refractive index, which is directly correlated to atomic density. We account for this effect in our analysis by scaling the heat capacity proportionally to the change in refractive index. As previously reported,[214] we expect no change in the longitudinal phonon velocity for the amorphous films in each sample set. Additionally, all of these film thicknesses were held constant at 50 ± 5 nm to negate any length scale effects. Accounting for all of these factors, we observe an increase in thermal conductivity with film density. This is reasonable given previous studies investigating the effects of reduced atomic density of the thermal conductivity of amorphous films.[206, 208, 214, 226]

To put the reduction in thermal conductivity due to the atomic density into perspective, we turn to the minimum limit to thermal conductivity.[99] This model has served as a baseline for comparing experimental data of amorphous systems for several

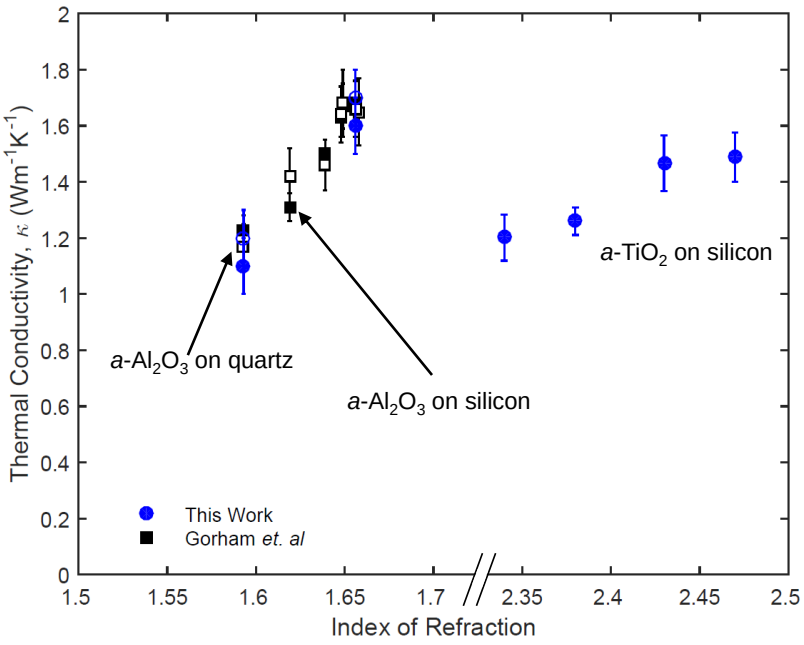

Figure 5.3: Thermal conductivity of both a-Al_2O_3 and a-TiO_2 as a function of refractive index, which directly corresponds to the atomic density. The film thickness across these samples was held constant, at 50 ± 5 nm. We account for the reduced heat capacity due to the change in density in our analysis and do not expect a change in the longitudinal phonon velocity, as shown in Gorham et. al.[214] Because of this, the data indicate that the strong density dependence of the thermal conductivity is an intrinsic property of amorphous Al_2O_3 and TiO_2.

decades. The minimum limit is given by

$$\kappa_{min} = \frac{\hbar^2}{6\pi^2 k_B T^2} \sum_j \int_0^{\omega_{c,j}} \tau_{min,j} \frac{\omega^4}{v_j} \frac{\exp(\frac{\hbar\omega}{k_B T})}{\left(\exp(\frac{\hbar\omega}{k_B T}) - 1\right)^2} d\omega \tag{5.2}$$

where $\kappa_{\min}$ is the minimum thermal conductivity, j is the phonon polarization index, $\tau_{\min}$ is the minimum scattering time, ω is the angular frequency, $\omega_{c,j}$ is the cut-off frequency, and v_j is the phonon group velocity. To evaluate Eq. 5.2 for our amorphous films, we take the longitudinal and transverse sound speeds for a-Al_2O_3 and a-TiO_2 from Ref. [214] and [231], respectively. Additionally, we use $n = 116.6$ nm^{-3} for the atomic density of Al_2O_3 and $n = 97.2$ nm^{-3} for TiO_2 in calculating the cut-off frequencies (where $\omega_{c,j} = v_j(6\pi^2 n)^{1/3}$). Our calculations of the minimum thermal

conductivity for a-Al_2O_3 and a-TiO_2 are shown in Fig. 5.4(a) and (b) as solid lines, and are consistent with the measured data for higher atomic densities (approaching bulk). However, the minimum limit over-predicts the thermal conductivity for lower atomic densities; instead, to account for density effects, we turn to a differential effective-medium (DEM) approximation,[206,232] which attempts to describe thermal properties in heterogeneous materials by considering a common "effective" medium between, in our case, the solid atoms and the additional "space" between the atoms (i.e., assumed here as vacuum). This model proposes that thermal conductivity scales with atomic density and is given by

$$\kappa_{min} = \kappa(\frac{n}{n_{bulk}})^{\frac{3}{2}} \tag{5.3}$$

For the a-TiO_2 films, we take κ as either 1.49 $Wm^{-1}K^{-1}$ from the maximum thermal conductivity measured in our film series or as the minimum limit calculated by Eq. 5.2; we assume n_{bulk} as 7.88 x 10^{28} atoms m^{-3}, which again corresponds to our highest density a-TiO_2 film. Based on earlier work relating the refractive index of a-TiO_2 to its density[183], we determine the atomic density according to n = $3N_{\text{A}}(2.86\tilde{n} - 3.63)/M$, where $\tilde{n}$ is the refractive index measured at 550 nm, N_{A} is Avogadro's number, and M is the molecular weight. For a-Al_2O_3, we take κ as either the calculated minimum limit or as 1.68 $Wm^{-1}K^{-1}$, the maximum thermal conductivity of a-Al_2O_3 that we measure; n_{bulk} as 9.25 x 10^{28} atoms m^{-3}, which corresponds to our highest density film; and $n = 5N_{\text{A}}(7.174\tilde{n} - 8.76)/M$, which is consistent with previous work studying density effects in amorphous alumina thin films.[214] We choose n_{bulk} and κ as the highest atomic density and thermal conductivity that we measure in each sample set to effectively normalize the data and better understand the observed trends.

Both DEM-based approximations are shown in Fig. 5.4(a) and (b) for a-TiO_2 and

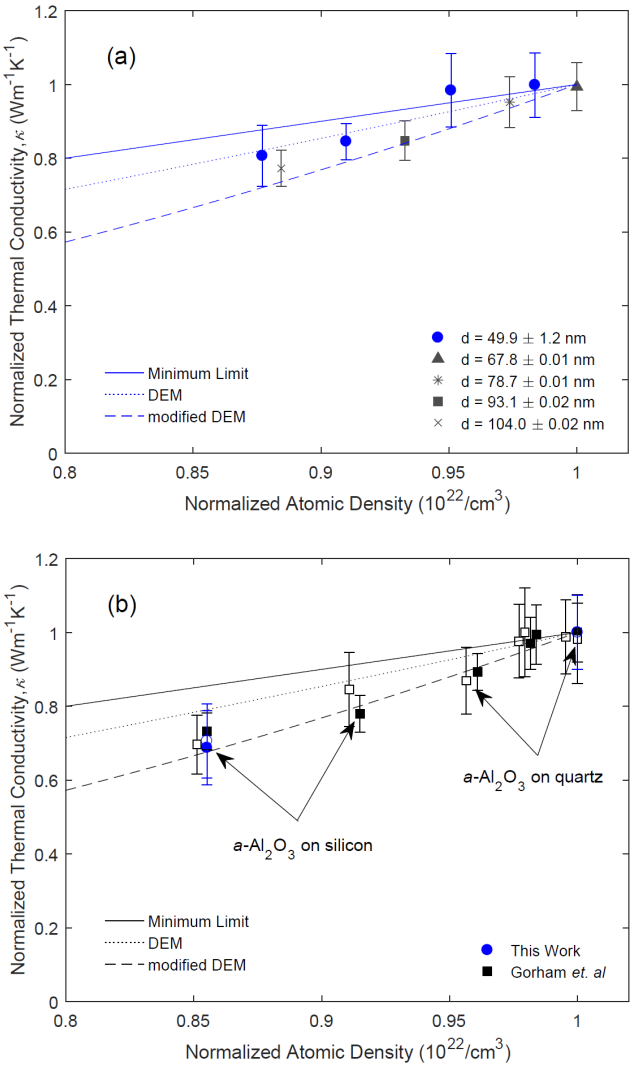

Figure 5.4: Normalized thermal conductivity of the (a) a-TiO_2 and (b) a-Al_2O_3 films as a function of normalized atomic density. The minimum limit is shown in dashed lines, the DEM approximation in dotted lines, and the DEM modified with the minimum limit in dashed lines. Normalizing the data provides better comparison with the various models. The minimum limit agrees somewhat with the higher density films, but fails to adequately describe the trends in thermal conductivity due to changes in density. In contrast, the DEM-based approximations agree much better with the data, and the minimum limit modified DEM model closely matches the trends. Additionally, we observe no size effects on the thermal conductivity of a-TiO_2 for films thicker than ~50 nm, as apparent from the general trends in thermal conductivity scaling with atomic density regardless of the film thickness (ranging from ~50–100 nm). All a-Al_2O_3 films shown in (b) have thicknesses of 50 ± 5 nm.

a-Al_2O_3, respectively, taking κ as either the calculated minimum limit (dashed lines) or as the measured value of the highest density film (dotted lines). Compared to the minimum limit prediction, the DEM exhibits much better agreement with the measured thermal conductivity data, and this approximation modified with the minimum limit predicts the trends in the experimental data particularly well. This approach is convenient because it requires only knowledge of sound velocity and atomic density, where the DEM calculation additionally involves knowledge of the thermal conductivity of the fully dense phase of the amorphous material. Previous reports have found similar agreement using this model to study low thermal conductivity materials,[208, 214] suggesting that this is a promising approach for predicting the thermal properties of amorphous thin films.

To further investigate the interplay between atomic density and film thickness, we examine a series of a-TiO_2 films in which both material parameters are varied. The thermal conductivity of these films of varying film thickness (~50-100 nm) is shown in Fig. 5.4(a). The data indicate that for amorphous films thicker than ~50 nm, the thickness contributes negligibly to thermal conductivity: within our uncertainty, we observe no change in κ due to film thickness, rather, the change in thermal conductivity is driven by the variation in atomic density.

5.4 Summary

In summary, we have measured the thermal conductivity of ALD-grown amorphous Al_2O_3 and TiO_2 thin films of varying film thicknesses and densities. For films less than ~50 nm, we measure an effective thermal conductivity which decreases with reduced film thickness. This is attributed to the increased effect of thermal boundary resistances with decreasing thickness. We determine a thickness- and substrate-independent intrinsic thermal conductivity using a series-resistor model and find that

our fitted values agree well with the literature. For films greater than ~50 nm, there is no significant dependence on film thickness or substrate. We measure the thermal conductivity due to a reduction in atomic density and observe a proportional relation. The density dependence of thermal conductivity of these amorphous films is well described by a differential effective medium approximation that is modified by a minimum limit model. We observe similar trends in both for *a*-Al_2O_3 and *a*-TiO_2, suggesting that the dependence of thermal conductivity on atomic density is an intrinsic property of amorphous thin films.

Chapter 6

Conclusions

6.1 Summary

Continuing advances in the technology of electronic devices makes it critical to understand thermal transport in the constituent materials. In particular, understanding the role that disorder and defects play on thermal conductivity is crucial to thermal management and device engineering. While near-perfect materials can be fabricated, this is often expensive and inefficient. Realistically, most of the materials that are suitable for use as constituents in devices will be prone to defects or even complete disorder; this should not be considered a flaw, but rather, an opportunity to take advantage of these mechanisms and cleverly engineer materials with the desired thermal properties.

In summary, Chapter 1 provided the motivation behind this work and described applications for which my research has particular relevance.

In Chapter 2, the various types of defects often present in materials were described, and the basic concepts behind phonon scattering and thermal conductivity were presented.

Chapter 3 discussed time-domain thermoreflectance (TDTR), the main experi-

ment used to measure the thermal properties of the thin films studied in this thesis. The two variants—two color and two tint—were described and the importance of consistently measuring calibration samples as a metric for TDTR testing was emphasized.

In Chapter 4, the role of crystalline coherence length on thermal conductivity in MgO thin films was presented. We observe a direct correlation between coherence length—the length scale governed by defects and dislocations in a material—and thermal conductivity, implying that these defects have a significant impact on phonon scattering.

Chapter 5 discussed density and length scale effects in amorphous Al_2O_3 and TiO_2 thin films. In the films less than ≤ 40 nm, the thermal resistance decreases as the film thickness is reduced, which is attributed to the increased influence of the interfaces with decreasing film thickness. In films ≥ 50 nm, the thermal conductivity is directly correlated to an increase in atomic density regardless of film thickness.

While limited, the scope of this work provides insight into the role that disorder plays on thermal conductivity and will hopefully motivate future studies to further investigate these mechanisms.

6.2 Future Work

There are several ideas and projects that could arise from the results presented here. The MgO work experimentally demonstrates the influence of defects and dislocations on the thermal conductivity of thin films, but does not contain the rigorous characterization necessary to quantify the density of defects and dislocations present in these thin films. Coupling in-depth characterization with a more thorough model could lend insight into the physics behind phonon interactions with point and line defects. Additionally, it would be intriguing to explore the idea of thermal rectification,

that is, altering the heat flow depending on the direction of measurement. A material engineered to contain a gradient of dislocations throughout the film thickness might scatter phonons preferentially depending on whether the flow of heat occurs from top to bottom or vice versa; this would manifest as a different experimentally-determined value of cross-plane thermal conductivity when measured from either direction.

While amorphous films possess no long-range order, thorough characterization could indicate the degree of short-range order. Pairing this with thermal conductivity measurements could offer insight into the different mechanisms that arise with varying degrees of short-range ordering in amorphous films. In addition, it would be interesting to determine whether thermal conductivity could be used as a metric for gaging the crystallinity of a thin film. For instance, during ALD growth, oxide thin films are no longer amorphous if deposited above a certain threshold temperature; if this amorphous-to-crystalline transition corresponds to an abrupt change in κ, this could point to the use of thermal conductivity measurements (particularly via TDTR, given its relatively high throughput) as a quick and efficient method for evaluating a film's crystallinity.

Bibliography

[1] C. Kittel, *Introduction to Solid State Physics*. John Wiley and Sons, 8th ed., 2004.

[2] S. O. Kasap, *Principles of Electronic Materials and Devices*. New York: McGraw-Hill, 3rd ed., 2006.

[3] W. D. Callister, *Materials Science and Engineering: An Introduction*. New York: John Wiley and Sons, 7th ed., 2007.

[4] F. Incropera and D. P. DeWitt, *Fundamentals of Heat and Mass Transfer*. New York: Wiley and Sons, Inc., 1996.

[5] G. D. Wilk, R. M. Wallace, and J. M. Anthony, "High-k gate dielectrics: Current status and materials properties considerations," *Journal of Applied Physics*, vol. 89, no. 10, pp. 5243–5275, 2001.

[6] C. M. Tanner, Y.-C. Perng, C. Frewin, S. E. Saddow, and J. P. Chang, "Electrical performance of Al_2O_3 gate dielectric films deposited by atomic layer deposition on 4H-SiC," *Applied Physics Letters*, vol. 91, no. 20, p. 203510, 2007.

[7] J. B. Kim, C. Fuentes-Hernandez, W. J. Potscavage, X.-H. Zhang, and B. Kippelen, "Low-voltage InGaZnO thin-film transistors with Al_2O_3 gate insulator grown by atomic layer deposition," *Applied Physics Letters*, vol. 94, no. 14, p. 142107, 2009.

[8] Y. Xuan, Y. Q. Wu, H. C. Lin, T. Shen, and P. D. Ye, "Submicrometer inversion-type enhancement-mode InGaAs MOSFET with atomic-layer-deposited Al_2O_3 as gate dielectric," *IEEE Electron Device Letters*, vol. 28, no. 11, pp. 935–938, 2007.

[9] P. D. Ye, B. Yang, K. K. Ng, J. Bude, G. D. Wilk, S. Halder, and J. C. M. Hwang, "GaN metal-oxide-semiconductor high-electron-mobility-transistor with atomic layer deposited Al_2O_3 as gate dielectric," *Applied Physics Letters*, vol. 86, no. 6, p. 063501, 2005.

[10] K. F. Albertin, M. A. Valle, and I. Pereyra, "Study of TiO_2 and SiO_2/TiO_2 as gate dielectric materials," *ECS Transactions*, vol. 4, no. 1, pp. 409–416, 2007.

[11] K. L. Chopra, "Avalanche-induced negative resistance in thin oxide films," *Journal of Applied Physics*, vol. 36, no. 1, pp. 184–187, 1965.

[12] L. Yan, C. M. Lopez, R. P. Shrestha, E. A. Irene, A. A. Suvorova, and M. Saunders, "Magnesium oxide as a candidate high-k gate dielectric," *Applied Physics Letters*, vol. 88, no. 14, p. 142901, 2006.

[13] M. D. Groner, F. H. Fabreguette, J. W. Elam, and S. M. George, "Low-temperature Al_2O_3 atomic layer deposition," *Chemistry of Materials*, vol. 16, no. 4, pp. 639–645, 2004.

[14] S. E. Potts, L. R. van den Elzen, G. Dingemans, E. Langereis, W. Keuning, M. C. van de Sanden, and W. M. Kessels, "Low temperature plasma-enhanced atomic layer deposition of metal oxide thin films," *Journal of the Electrochemical Society*, vol. 25, no. 4, pp. 233–242, 2010.

[15] G. T. Furukawa, T. B. Douglas, R. E. McCoskey, and D. C. Ginnings, "Thermal properties of aluminum oxide from 0 to 1200K," *Journal of Research of the National Bureau of Standards*, vol. 57, no. 2, pp. 67–82, 1956.

[16] R. Heid, D. Strauch, and K. P. Bohnen, "*Ab initio* lattice dynamics of sapphire," *Physical Review B*, vol. 61, no. 13, pp. 8625–8627, 2000.

[17] D.-A. Borca-Tasciuc and G. Chen, "Anisotropic thermal properties of nanochanneled alumina templates," *Journal of Applied Physics*, vol. 97, no. 8, p. 084303, 2005.

[18] H. Takikawa, T. Matsui, T. Sakakibara, A. Bendavid, and P. J. Martin, "Properties of titanium oxide film prepared by reactive cathodic vacuum arc deposition," *Thin Solid Films*, vol. 348, no. 1–2, pp. 145–151, 1999.

[19] A. C. Dillon, A. W. Ott, J. D. Way, and S. M. George, "Surface chemistry of Al_2O_3 deposition using $Al(CH_3)_2$ and H_2O in a binary reaction sequence," *Surface Science*, vol. 322, no. 1, pp. 230–242, 1995.

[20] A. W. Ott, J. W. Klaus, J. M. Johnson, and S. M. George, "Al_2O_3 thin film growth on Si(100) using binary reaction sequence chemistry," *Thin Solid Films*, vol. 292, no. 1, pp. 135–144, 1997.

[21] J. W. Elam, M. D. Groner, and S. M. George, "Viscous flow reactor with quartz crystal microbalance for thin film growth by atomic layer deposition," *Review of Scientific Instruments*, vol. 73, no. 8, pp. 2981–2987, 2002.

[22] M. D. Groner, J. W. Elam, F. H. Fabreguette, and S. M. George, "Electrical characterization of thin Al_2O_3 films grown by atomic layer deposition on silicon and various metal substrates," *Thin Solid Films*, vol. 413, no. 1–2, pp. 186–197, 2002.

[23] S. J. Yun, K.-H. Lee, J. Skarp, H.-R. Kim, and K.-S. Nam, "Dependence of atomic layer-deposited Al_2O_3 films characteristics on growth temperature and al precursors of $Al(CH_3)_2$ and $AlCl_3$," *Journal of Vacuum Science & Technology A*, vol. 15, no. 6, pp. 2993–2997, 1997.

[24] R. Matero, A. Rahtu, M. Ritala, M. Leskelä, and T. Sajavaara, "Effect of water dose on the atomic layer deposition rate of oxide thin films," *Thin Solid Films*, vol. 368, no. 1, pp. 1–7, 2000.

[25] K. Kukli, M. Ritala, M. Leskelä, and J. Jokinen, "Atomic layer epitaxy growth of aluminum oxide thin films from a novel $Al(CH_3)_2Cl$ precursor and H_2O," *Journal of Vacuum Science & Technology A*, vol. 15, no. 4, pp. 2214–2218, 1997.

[26] F. Jia-Fa, S. Koji, and T. Koichi, "Low-temperature growth of thin films of Al_2O_3 by sequential surface chemical reaction of trimethylaluminum and H_2O_2," *Japanese Journal of Applied Physics*, vol. 30, no. 6B, p. L1139, 1991.

[27] V. E. Drozd, A. P. Baraban, and I. O. Nikiforova, "Electrical properties of Si—Al_2O_3 structures grown by ml-ale," *Applied Surface Science*, vol. 82, pp. 583–586, 1994.

[28] G. Balakrishnan, P. Kuppusami, S. T. Sundari, R. Thirumurugesan, V. Ganesan, E. Mohandas, and D. Sastikumar, "Structural and optical properties of γ-alumina thin films prepared by pulsed laser deposition," *Thin Solid Films*, vol. 518, no. 14, pp. 3898–3902, 2010.

[29] K. S. Shamala, L. C. S. Murthy, M. C. Radhakrishna, and K. N. Rao, "Characterization of Al_2O_3 thin films prepared by spray pyrolysis method for humidity sensor," *Sensors and Actuators A: Physical*, vol. 135, no. 2, pp. 552–557, 2007.

[30] K. Marszałek, P. Winkowski, and J. Jaglarz, "Optical properties of the Al_2O_3/SiO_2 and $Al_2O_3/HfO_2/SiO_2$ antireflective coatings," *Materials Science-Poland*, vol. 32, no. 1, pp. 80–87, 2014.

[31] E. F. Schubert, M. Passlack, M. Hong, J. Mannerts, R. L. Opila, L. N. Pfeiffer, K. W. West, C. G. Bethea, and G. J. Zydzik, "Properties of Al_2O_3 optical

coatings on GaAs produced by oxidation of epitaxial AlAs/GaAs films," *Applied Physics Letters*, vol. 64, no. 22, pp. 2976–2978, 1994.

[32] P. Katiyar, C. Jin, and R. J. Narayan, "Electrical properties of amorphous aluminum oxide thin films," *Acta Materialia*, vol. 53, no. 9, pp. 2617–2622, 2005.

[33] M. M. Aslan, N. A. Webster, C. L. Byard, M. B. Pereira, C. M. Hayes, R. S. Wiederkehr, and S. B. Mendes, "Low-loss optical waveguides for the near ultraviolet and visible spectral regions with Al_2O_3 thin films from atomic layer deposition," *Thin Solid Films*, vol. 518, no. 17, pp. 4935–4940, 2010.

[34] G. Este and W. D. Westwood, "Reactive deposition of low loss Al_2O_3 optical waveguides by modified dc planar magnetron sputtering," *Journal of Vacuum Science & Technology A*, vol. 2, no. 3, pp. 1238–1247, 1984.

[35] Q. Y. Zhang, P. S. Wang, W. J. Zhao, and L. Wang, "Ion beam assisted deposition of Al_2O_3 optical waveguides on silicon," *Surface and Coatings Technology*, vol. 128–129, pp. 121–125, 2000.

[36] J. Masalski, J. Gluszek, J. Zabrzeski, K. Nitsch, and P. Gluszek, "Improvement in corrosion resistance of the 316l stainless steel by means of Al_2O_3 coatings deposited by the sol-gel method," *Thin Solid Films*, vol. 349, no. 1–2, pp. 186–190, 1999.

[37] S. Zhu, F. Wang, H. Lou, and W. Wu, "Reactive sputter deposition of alumina films on superalloys and their high-temperature corrosion resistance," *Surface and Coatings Technology*, vol. 71, no. 1, pp. 9–15, 1995.

[38] F. Guidi, G. Moretti, G. Carta, M. Natali, G. Rossetto, Z. Pierino, G. Salmaso, and V. Rigato, "Electrochemical anticorrosion performance evaluation of Al_2O_3

coatings deposited by MOCVD on an industrial brass substrate," *Electrochimica Acta*, vol. 50, no. 23, pp. 4609–4614, 2005.

[39] L. Juhász and J. Mizsei, "Humidity sensor structures with thin film porous alumina for on-chip integration," *Thin Solid Films*, vol. 517, no. 22, pp. 6198–6201, 2009.

[40] Y.-S. Chaug and N. Roy, "Reactions at the aluminum oxide-ferrite interface," *Thin Solid Films*, vol. 193, pp. 959–964, 1990.

[41] M. Furuhashi, M. Fujiwara, T. Ohshiro, M. Tsutsui, K. Matsubara, M. Taniguchi, S. Takeuchi, and T. Kawai, "Development of microfabricated TiO_2 channel waveguides," *AIP Advances*, vol. 1, no. 3, p. 032102, 2011.

[42] D. W. Dobbs, I. Gershkovich, and B. T. Cunningham, "Fabrication of a graded-wavelength guided-mode resonance filter photonic crystal," *Applied Physics Letters*, vol. 89, no. 12, p. 123113, 2006.

[43] T. Alasaarela, D. Zheng, L. Huang, A. Priimagi, B. Bai, A. Tervonen, S. Honkanen, M. Kuittinen, and J. Turunen, "Single-layer one-dimensional nonpolarizing guided-mode resonance filters under normal incidence," *Optics Letters*, vol. 36, no. 13, pp. 2411–2413, 2011.

[44] M. R. Saleem, P. Stenberg, T. Alasaarela, P. Silfsten, M. B. Khan, S. Honkanen, and J. Turunen, "Towards a thermal organic-inorganic guided mode resonance filters," *Optics Express*, vol. 19, no. 24, pp. 24241–24251, 2011.

[45] M. R. Saleem, D. Zheng, B. Bai, P. Stenberg, M. Kuittinen, S. Honkanen, and J. Turunen, "Replicable one-dimensional non-polarizing guided mode resonance gratings under normal incidence," *Optics Express*, vol. 20, no. 15, pp. 16974–16980, 2012.

[46] S. Hu, M. R. Shaner, J. A. Beardslee, M. Lichterman, B. S. Brunschwig, and N. S. Lewis, "Amorphous TiO_2 coatings stabilize Si, GaAs, and GaP photoanodes for efficient water oxidation," *Science*, vol. 344, no. 6187, pp. 1005–1009, 2014.

[47] Y.-Q. Wang, S.-G. Chen, X.-H. Tang, O. Palchik, A. Zaban, Y. Koltypin, and A. Gedanken, "Mesoporous titanium dioxide: sonochemical synthesis and application in dye-sensitized solar cells," *Journal of Materials Chemistry*, vol. 11, no. 2, pp. 521–526, 2001.

[48] U. Bach, D. Lupo, P. Comte, J. E. Moser, F. Weissortel, J. Salbeck, H. Spreitzer, and M. Gratzel, "Solid-state dye-sensitized mesoporous TiO_2 solar cells with high photon-to-electron conversion efficiencies," *Nature*, vol. 395, no. 6702, pp. 583–585, 1998.

[49] N. G. Park, J. van de Lagemaat, and A. J. Frank, "Comparison of dye-sensitized rutile- and anatase-based TiO_2 solar cells," *The Journal of Physical Chemistry B*, vol. 104, no. 38, pp. 8989–8994, 2000.

[50] F. Argall, "Switching phenomena in titanium oxide thin films," *Solid-State Electronics*, vol. 11, no. 5, pp. 535–541, 1968.

[51] B. J. Choi, D. S. Jeong, S. K. Kim, C. Rohde, S. Choi, J. H. Oh, H. J. Kim, C. S. Hwang, K. Szot, R. Waser, B. Reichenberg, and S. Tiedke, "Resistive switching mechanism of TiO_2 thin films grown by atomic-layer deposition," *Journal of Applied Physics*, vol. 98, no. 3, p. 033715, 2005.

[52] A. Posadas, F. J. Walker, C. H. Ahn, T. L. Goodrich, Z. Cai, and K. S. Ziemer, "Epitaxial MgO as an alternative gate dielectric for SiC transistor applications," *Applied Physics Letters*, vol. 92, no. 23, p. 233511, 2008.

[53] S. S. P. Parkin, C. Kaiser, A. Panchula, P. M. Rice, B. Hughes, M. Samant, and S.-H. Yang, "Giant tunnelling magnetoresistance at room temperature with MgO (100) tunnel barriers," *Nat Mater*, vol. 3, no. 12, pp. 862–867, 2004.

[54] S. Yuasa, T. Nagahama, A. Fukushima, Y. Suzuki, and K. Ando, "Giant room-temperature magnetoresistance in single-crystal Fe/MgO/Fe magnetic tunnel junctions," *Nat Mater*, vol. 3, no. 12, pp. 868–871, 2004.

[55] W. Schottky, "Über den mechanismus der ionenbewegung in festen elektrolyten," *Zeitschrift fur physikalishce Chemie B*, vol. 29, pp. 335–355, 1935.

[56] J. Frenkel, "Über die wärmebewegung in festen und flüssigen körpern," *Zeitschrift fur Physik*, vol. 35, no. 8, pp. 652–669, 1926.

[57] J. M. Burgers, *Physics. — Some considerations on the fields of stress connected with dislocations in a regular crystal lattice. I*, pp. 335–389. Dordrecht: Springer Netherlands, 1995.

[58] J. F. Ihlefeld, J. C. Ginn, D. J. Shelton, V. Matias, M. A. Rodriguez, P. G. Kotula, J. F. Carroll, G. D. Boreman, P. G. Clem, and M. B. Sinclair, "Crystal coherence length effects on the infrared optical response of MgO thin films," *Applied Physics Letters*, vol. 97, no. 19, p. 191913, 2010.

[59] K. E. Meyer, R. Cheaito, E. Paisley, C. T. Shelton, J. L. Braun, J.-P. Maria, J. F. Ihlefeld, and P. E. Hopkins, "Crystalline coherence length effects on the thermal conductivity of MgO thin films," *Journal of Materials Science*, pp. 1–10, 2016.

[60] A. Einstein, "Die plancksche theorie der strahlung und die theorie der spezifischen wärme," *Annalen der Physik*, vol. 327, no. 1, pp. 180–190, 1906.

[61] A. Einstein, "Elementare betrachtungen über die thermische molekularbewegung in festen körpern," *Annalen der Physik*, vol. 35, 1911.

[62] H. F. Weber, "Die specifische wärme des kohlenstoffs," *Annalen der Physik*, vol. 223, no. 10, pp. 311–319, 1872.

[63] H. F. Weber, "Die specifischen wärmen der elemente kohlenstoff, bor und silicium," *Annalen der Physik*, vol. 230, no. 3, pp. 367–423, 1875.

[64] P. Debye, "Zur theorie der spezifischen wärmen," *Annalen der Physik*, vol. 344, no. 14, pp. 789–839, 1912.

[65] P. A. M. Dirac, "The quantum theory of the emission and absorption of radiation," *Proceedings of the Royal Society of London A: Mathematical, Physical and Engineering Sciences*, vol. 114, no. 767, pp. 243–265, 1927.

[66] I. Tamm, "Über die quantentheorie der molekularen lichtstreuung in festen körpern," *Zeitschrift fur Physik*, vol. 60, pp. 345–363, 1930.

[67] J. Frenkel, *Wave Mechanics: Elementary Theory*. Oxford University Press, 1932.

[68] G. P. Srivastava, *The Physics of Phonons*. New York: Taylor & Francis, 1990.

[69] J. W. Lynn, H. G. Smith, and R. M. Nicklow, "Lattice dynamics of gold," *Physical Review B*, vol. 8, no. 8, pp. 3493–3499, 1973.

[70] M. J. L. Sangster, G. Peckham, and D. H. Saunderson, "Lattice dynamics of magnesium oxide," *Journal of Physics C: Solid State Physics*, vol. 3, no. 5, pp. 1026–1036, 1970.

[71] K. Momma and F. Izumi, "Vesta: a three-dimensional visualization system for electronic and structural analysis," *Journal of Applied Crystallography*, vol. 41, no. 3, pp. 653–658, 2008.

[72] K. Momma and F. Izumi, "Vesta 3 for three-dimensional visualization of crystal, volumetric and morphology data," *Journal of Applied Crystallography*, vol. 44, no. 6, pp. 1272–1276, 2011.

[73] M. G. Holland, "Analysis of lattice thermal conductivity," *Physical Review*, vol. 132, no. 6, pp. 2461–2471, 1963.

[74] J. D. Chung, A. J. H. McGaughey, and M. Kaviany, "Role of phonon dispersion in lattice thermal conductivity modeling," *Journal of Heat Transfer*, vol. 126, no. 3, pp. 376–380, 2004.

[75] R. Yang and G. Chen, "Thermal conductivity modeling of periodic two-dimensional nanocomposites," *Physical Review B*, vol. 69, no. 19, p. 195316, 2004.

[76] P. E. Hopkins, J. C. Duda, and P. M. Norris, "Anharmonic phonon interactions at interfaces and contributions to thermal boundary conductance," *Journal of Heat Transfer*, vol. 133, no. 6, pp. 062401–062401, 2011.

[77] C. Dames and G. Chen, "Theoretical phonon thermal conductivity of Si/Ge superlattice nanowires," *Journal of Applied Physics*, vol. 95, no. 2, pp. 682–693, 2004.

[78] Z. Wang, J. E. Alaniz, W. Jang, J. E. Garay, and C. Dames, "Thermal conductivity of nanocrystalline silicon: Importance of grain size and frequency-dependent mean free paths," *Nano Letters*, vol. 11, no. 6, pp. 2206–2213, 2011.

[79] E. Pop, R. W. Dutton, and K. E. Goodson, "Analytic band Monte Carlo model for electron transport in Si including acoustic and optical phonon dispersion," *Journal of Applied Physics*, vol. 96, no. 9, pp. 4998–5005, 2004.

[80] R. Peierls, "Zur kinetischen theorie der wärmeleitung in kristallen," *Annalen der Physik*, vol. 395, no. 8, pp. 1055–1101, 1929.

[81] P. G. Klemens, "The scattering of low-frequency lattice waves by static imperfections," *Proceedings of the Physical Society. Section A*, vol. 68, no. 12, p. 1113, 1955.

[82] J. Callaway, "Model for lattice thermal conductivity at low temperatures," *Physical Review*, vol. 113, no. 4, pp. 1046–1051, 1959.

[83] M. Asheghi, Y. K. Leung, S. S. Wong, and K. E. Goodson, "Phonon-boundary scattering in thin silicon layers," *Applied Physics Letters*, vol. 71, no. 13, pp. 1798–1800, 1997.

[84] Y. Touloukian, R. Powell, C. Ho, and P. Klemens, *Thermophysical Properties of Matter - Specific Heat: Nonmetallic Solids*, vol. 5. New York: IFI/Plenum, 1970.

[85] G. A. Slack, "Thermal conductivity of MgO, Al_2O_3, $MgAl_2O_4$, and Fe_3O_4 crystals from 3 to 300 K," *Phys. Rev.*, vol. 126, pp. 427–441, Apr 1962.

[86] B. F. Donovan, B. M. Foley, J. F. Ihlefeld, J.-P. Maria, and P. E. Hopkins, "Spectral phonon scattering effects on the thermal conductivity of nano-grained barium titanate," *Applied Physics Letters*, vol. 105, no. 8, p. 082907, 2014.

[87] B. M. Foley, H. J. Brown-Shaklee, J. C. Duda, R. Cheaito, B. J. Gibbons, D. Medlin, J. F. Ihlefeld, and P. E. Hopkins, "Thermal conductivity of nano-grained $SrTiO_3$ thin films," *Applied Physics Letters*, vol. 101, no. 23, p. 231908, 2012.

[88] P. G. Klemens, "Phonon scattering and thermal resistance due to grain boundaries," *International Journal of Thermophysics*, vol. 15, no. 6, pp. 1345–1351, 1994.

[89] A. Jeżowski, J. Mucha, R. Pazik, and W. Strek, "Influence of crystallite size on the thermal conductivity in $BaTiO_3$ nanoceramics," *Applied Physics Letters*, vol. 90, no. 11, p. 114104, 2007.

[90] R. Berman, "The thermal conductivity of some polycrystalline solids at low temperatures," *Proceedings of the Physical Society. Section A*, vol. 65, no. 12, p. 1029, 1952.

[91] J. Callaway and H. C. von Baeyer, "Effect of point imperfections on lattice thermal conductivity," *Physical Review*, vol. 120, no. 4, pp. 1149–1154, 1960.

[92] P. G. Klemens, *Lattice Thermal Resistivity due to Point Defects*, pp. 15–20. Boston, MA: Springer US, 1983.

[93] B. Abeles, "Lattice thermal conductivity of disordered semiconductor alloys at high temperatures," *Physical Review*, vol. 131, no. 5, pp. 1906–1911, 1963.

[94] C. A. Ratsifaritana and P. G. Klemens, "Scattering of phonons by vacancies," *International Journal of Thermophysics*, vol. 8, no. 6, pp. 737–750, 1987.

[95] Y. Ni, S. Xiong, S. Volz, and T. Dumitrica, "Thermal transport along the dislocation line in silicon carbide," *Physical Review Letters*, vol. 113, p. 124301, 2014.

[96] M. Eden, "Nmr studies of oxide-based glasses," *Annual Reports Section "C" (Physical Chemistry)*, vol. 108, no. 1, pp. 177–221, 2012.

[97] P. B. Allen, J. L. Feldman, J. Fabian, and F. Wooten, "Diffusons, locons and propagons: Character of atomic vibrations in amorphous Si," *Philosophical Magazine Part B*, vol. 79, no. 11-12, pp. 1715–1731, 1999.

[98] D. G. Cahill and R. O. Pohl, "Heat flow and lattice vibrations in glasses," *Solid State Communications*, vol. 70, no. 10, pp. 927–930, 1989.

[99] D. G. Cahill, S. K. Watson, and R. O. Pohl, "Lower limit to the thermal conductivity of disordered crystals," *Physical Review B*, vol. 46, no. 10, pp. 6131–6140, 1992.

[100] E. T. Swartz and R. O. Pohl, "Thermal boundary resistance," *Reviews of Modern Physics*, vol. 61, no. 3, 1989.

[101] P. L. Kapitza, "Heat transfer and superfluidity of Helium II," *Phys. Rev.*, vol. 60, pp. 354–355, Aug 1941.

[102] C. Monachon and L. Weber, "Influence of a nanometric Al_2O_3 interlayer on the thermal conductance of an Al/(Si, Diamond) interface," *Advanced Engineering Materials*, vol. 17, no. 1, pp. 68–75, 2015.

[103] P. E. Hopkins, "Thermal transport across solid interfaces with nanoscale imperfections: Effects of roughness, disorder, dislocations, and bonding on thermal boundary conductance," *ISRN Mechanical Engineering*, vol. 2013, no. 682586, 2013.

[104] R. Cheaito, J. T. Gaskins, M. E. Caplan, B. F. Donovan, B. M. Foley, A. Giri, J. C. Duda, C. J. Szwejkowski, C. Constantin, H. J. Brown-Shaklee, J. F. Ihlefeld, and P. E. Hopkins, "Thermal boundary conductance accumulation and interfacial phonon transmission: Measurements and theory," *Physical Review B*, vol. 91, no. 3, p. 035432, 2015.

[105] R. M. Costescu, M. A. Wall, and D. G. Cahill, "Thermal conductance of epitaxial interfaces," *Physical Review B*, vol. 67, no. 5, p. 054302, 2003.

[106] R. B. Wilson, B. A. Apgar, W.-P. Hsieh, L. W. Martin, and D. G. Cahill, "Thermal conductance of strongly bonded metal-oxide interfaces," *Physical Review B*, vol. 91, no. 11, p. 115414, 2015.

[107] R. J. Stoner and H. J. Maris, "Kapitza conductance and heat flow between solids at temperatures from 50 to 300 K," *Physical Review B*, vol. 48, no. 22, pp. 16373–16387, 1993.

[108] P. E. Hopkins, R. N. Salaway, R. J. Stevens, and P. M. Norris, "Temperature-dependent thermal boundary conductance at Al/Al_2O_3 and Pt/Al_2O_3 interfaces," *International Journal of Thermophysics*, vol. 28, no. 3, pp. 947–957, 2007.

[109] R. J. Stevens, A. N. Smith, and P. M. Norris, "Measurement of thermal boundary conductance of a series of metal-dielectric interfaces by the transient thermoreflectance technique," *Journal of Heat Transfer*, vol. 127, no. 3, pp. 315–322, 2005.

[110] H.-K. Lyeo and D. G. Cahill, "Thermal conductance of interfaces between highly dissimilar materials," *Physical Review B*, vol. 73, no. 14, p. 144301, 2006.

[111] J. C. Duda, C.-Y. P. Yang, B. M. Foley, R. Cheaito, D. L. Medlin, R. E. Jones, and P. E. Hopkins, "Influence of interfacial properties on thermal transport at gold:silicon contacts," *Applied Physics Letters*, vol. 102, no. 8, p. 081902, 2013.

[112] P. M. Norris, N. Q. Le, and C. H. Baker, "Tuning phonon transport: From interfaces to nanostructures," *Journal of Heat Transfer*, vol. 135, no. 6, pp. 061604–061604, 2013.

[113] B. F. Donovan, C. J. Szwejkowski, J. C. Duda, R. Cheaito, J. T. Gaskins, C.-Y. Peter Yang, C. Constantin, R. E. Jones, and P. E. Hopkins, "Thermal boundary conductance across metal-gallium nitride interfaces from 80 to 450 K," *Applied Physics Letters*, vol. 105, no. 20, p. 203502, 2014.

[114] A. J. Schmidt, X. Chen, and G. Chen, "Pulse accumulation, radial heat conduction, and anisotropic thermal conductivity in pump-probe transient thermoreflectance," *Review of Scientific Instruments*, vol. 79, no. 11, p. 114902, 2008.

[115] A. J. Schmidt, "Pump-probe thermoreflectance," *Annual Review of Heat Transfer*, vol. 16, pp. 159–181, 2013.

[116] R. Rosei and D. W. Lynch, "Thermomodulation spectra of Al, Au, and Cu," *Physical Review B*, vol. 5, no. 10, pp. 3883–3894, 1972.

[117] C. A. Paddock and G. L. Eesley, "Transient thermoreflectance from thin metal films," *Journal of Applied Physics*, vol. 60, no. 1, pp. 285–290, 1986.

[118] D. G. Cahill, K. Goodson, and A. Majumdar, "Thermometry and thermal transport in micro/nanoscale solid-state devices and structures," *Journal of Heat Transfer*, vol. 124, no. 2, pp. 223–241, 2001.

[119] W. S. Capinski and H. J. Maris, "Improved apparatus for picosecond pump-and-probe optical measurements," *Review of Scientific Instruments*, vol. 67, no. 8, pp. 2720–2726, 1996.

[120] G. L. Eesley, "Generation of nonequilibrium electron and lattice temperatures in copper by picosecond laser pulses," *Physical Review B*, vol. 33, no. 4, pp. 2144–2151, 1986.

[121] P. E. Hopkins, P. M. Norris, and R. J. Stevens, "Influence of inelastic scattering at metal-dielectric interfaces," *Journal of Heat Transfer*, vol. 130, no. 2, pp. 022401–022401, 2008.

[122] R. Cheaito, *The Role of Size Effects on the Thermal Conductivity of Thin Film Alloys and Superlattices*. Thesis, University of Virginia, 2015.

[123] B. Foley, *Dynamic Control of Thermal Transport via Phonon Scattering at Ferroelastic Domain Walls*. Thesis, University of Virginia, 2016.

[124] B. Saleh and M. Teich, *Fundamentals of Photonics*. Wiley Series in Pure and Applied Optics, Wiley, 2013.

[125] Y. Wang, J. Y. Park, Y. K. Koh, and D. G. Cahill, "Thermoreflectance of metal transducers for time-domain thermoreflectance," *Journal of Applied Physics*, vol. 108, no. 4, p. 043507, 2010.

[126] R. Cheaito, C. S. Gorham, A. Misra, K. Hattar, and P. E. Hopkins, "Thermal conductivity measurements via time-domain thermoreflectance for the characterization of radiation induced damage," *Journal of Materials Research*, vol. 30, no. 9, pp. 1403–1412, 2015.

[127] M. Ghotbi, M. Ebrahim-Zadeh, A. Majchrowski, E. Michalski, and I. V. Kityk, "High-average-power femtosecond pulse generation in the blue using BiB_3O_6," *Optics Letters*, vol. 29, no. 21, pp. 2530–2532, 2004.

[128] D. G. Cahill, "Analysis of heat flow in layered structures for time-domain thermoreflectance," *Review of Scientific Instruments*, vol. 75, no. 12, 2004.

[129] A. J. Schmidt, *Optical characterization of thermal transport from the nanoscale to the macroscale*. Thesis, Massachussetts Institute of Technology, 2008.

[130] A. M. D. G. Cahill, K. Goodson, "Thermometry and thermal transport in micro/nanoscale solid-state devices and structures," *Journal of Heat Transfer*, vol. 124, no. 223, 2002.

[131] P. E. Hopkins, J. R. Serrano, L. M. Phinney, S. P. Kearney, T. W. Grasser, and C. T. Harris, "Criteria for cross-plane dominated thermal transport in multilayer thin film systems during modulated laser heating," *Journal of Heat Transfer*, vol. 132, no. 8, pp. 081302–081302, 2010.

[132] L. Wang, R. Cheaito, J. L. Braun, A. Giri, and P. E. Hopkins, "Thermal conductivity measurements of non-metals via combined time- and frequency-domain thermoreflectance without a metal film transducer," *Review of Scientific Instruments*, vol. 87, no. 9, p. 094902, 2016.

[133] T. Q. Qiu, T. Juhasz, C. Suarez, W. E. Bron, and C. L. Tien, "Femtosecond laser heating of multi-layer metals—II. Experiments," *International Journal of Heat and Mass Transfer*, vol. 37, no. 17, pp. 2799–2808, 1994.

[134] T. Q. Qiu and C. L. Tien, "Femtosecond laser heating of multi-layer metals—I. Analysis," *International Journal of Heat and Mass Transfer*, vol. 37, no. 17, pp. 2789–2797, 1994.

[135] S. I. Ansimov, B. L. Kapeliovich, and T. L. Perel'man, "Electron emission from metal surfaces exposed to ultrashort laser pulses," *Journal of Experimental and Theoretical Physics*, vol. 66, pp. 776–781, 1974.

[136] P. M. Norris, A. P. Caffrey, R. J. Stevens, J. M. Klopf, J. T. McLeskey, and A. N. Smith, "Femtosecond pump–probe nondestructive examination of materials (invited)," *Review of Scientific Instruments*, vol. 74, no. 1, pp. 400–406, 2003.

[137] H. E. Elsayed-Ali, T. B. Norris, M. A. Pessot, and G. A. Mourou, "Time-resolved observation of electron-phonon relaxation in copper," *Physical Review Letters*, vol. 58, no. 12, pp. 1212–1215, 1987.

[138] A. Giri, J. T. Gaskins, B. M. Foley, R. Cheaito, and P. E. Hopkins, "Experimental evidence of excited electron number density and temperature effects on electron-phonon coupling in gold films," *Journal of Applied Physics*, vol. 117, no. 4, p. 044305, 2015.

[139] C. Thomsen, H. T. Grahn, H. J. Maris, and J. Tauc, "Surface generation and detection of phonons by picosecond light pulses," *Physical Review B*, vol. 34, no. 6, pp. 4129–4138, 1986.

[140] C. Thomsen, J. Strait, Z. Vardeny, H. J. Maris, J. Tauc, and J. J. Hauser, "Coherent phonon generation and detection by picosecond light pulses," *Physical Review Letters*, vol. 53, no. 10, pp. 989–992, 1984.

[141] C. S. Gorham, K. Hattar, R. Cheaito, J. C. Duda, J. T. Gaskins, T. E. Beechem, J. F. Ihlefeld, L. B. Biedermann, E. S. Piekos, D. L. Medlin, and P. E. Hopkins, "Ion irradiation of the native oxide/silicon surface increases the thermal boundary conductance across aluminum/silicon interfaces," *Physical Review B*, vol. 90, p. 024301, 2014.

[142] G. Tas, J. J. Loomis, H. J. Maris, A. A. Bailes, and L. E. Seiberling, "Picosecond ultrasonics study of the modification of interfacial bonding by ion implantation," *Applied Physics Letters*, vol. 72, no. 18, pp. 2235–2237, 1998.

[143] M. D. Losego, M. E. Grady, N. R. Sottos, D. G. Cahill, and P. V. Braun, "Effects of chemical bonding on heat transport across interfaces," *Nat Mater*, vol. 11, no. 6, pp. 502–506, 2012.

[144] C. Thomsen, H. J. Maris, and J. Tauc, "Picosecond acoustics as a non-destructive tool for the characterization of very thin films," *Thin Solid Films*, vol. 154, no. 1, pp. 217–223, 1987.

[145] P. E. Hopkins, B. Kaehr, L. M. Phinney, T. P. Koehler, A. M. Grillet, D. Dunphy, F. Garcia, and C. J. Brinker, "Measuring the thermal conductivity of porous, transparent SiO_2 films with time domain thermoreflectance," *Journal of Heat Transfer*, vol. 133, no. 6, pp. 061601–061601, 2011.

[146] R. G. Morris and J. G. Hust, "Thermal conductivity measurements of silicon from 30° to 425°C," *Physical Review*, vol. 124, no. 5, pp. 1426–1430, 1961.

[147] D. G. Cahill, S.-M. Lee, and T. I. Selinder, "Thermal conductivity of κ-Al_2O_3 and α-Al_2O_3 wear-resistant coatings," *Journal of Applied Physics*, vol. 83, no. 11, pp. 5783–5786, 1998.

[148] J. H. Lienhard and J. H. Lienhard, *A Heat Transfer Textbook*. Courier Dover Publications, 4th ed., 2012.

[149] R. C. Weast, M. J. Astle, and W. H. Beyer, *CRC Handbook of Chemistry and Physics*, vol. 69. Boca Raton, FL: CRC Press, 1988.

[150] D.-W. Oh, C. Ko, S. Ramanathan, and D. G. Cahill, "Thermal conductivity and dynamic heat capacity across the metal-insulator transition in thin film VO_2," *Applied Physics Letters*, vol. 96, no. 15, p. 151906, 2010.

[151] J. Liu, J. Zhu, M. Tian, X. Gu, A. Schmidt, and R. Yang, "Simultaneous measurement of thermal conductivity and heat capacity of bulk and thin film materials using frequency-dependent transient thermoreflectance method," *Review of Scientific Instruments*, vol. 84, no. 3, p. 034902, 2013.

[152] A. M. Marconet, M. Asheghi, and K. E. Goodson, "From the casimir limit to phononic crystals: Twenty years of phonon transport studies using silicon-on-insulator technology," *Journal of Heat Transfer*, vol. 135, p. 061601, 2013.

[153] R. Cheaito, J. C. Duda, T. E. Beechem, K. Hattar, J. F. Ihlefeld, D. L. Medlin, M. A. Rodriguez, M. J. Campion, E. S. Piekos, and P. E. Hopkins, "Experimental investigation of size effects on the thermal conductivity of silicon-germanium alloy thin films," *Physical Review Letters*, vol. 109, p. 195901, 2012.

[154] M. J. Bierman, Y. K. A. Lau, A. V. Kvit, A. L. Schmitt, and S. Jin, "Dislocation-driven nanowire growth and Eshelby twist," *Science*, vol. 320, pp. 1060–1063, 2008.

[155] B. W. Jacobs, M. A. Crimp, K. McElroy, and V. M. Ayres, "Nanopipes in gallium nitride nanowires and rods," *Nano Letters*, vol. 8, pp. 4353–4358, 2008.

[156] J. Zhu, H. Peng, A. F. Marshall, D. M. Barnett, W. D. Nix, and Y. Cui, "Formation of chiral branched nanowires by the Eshelby twist," *Nature Nanotechnology*, vol. 3, pp. 477–481, 2008.

[157] S. A. Morin and S. Jin, "Screw dislocation-driven epitaxial solution growth of ZnO nanowires seeded by dislocations in gan substrates," *Nano Letters*, vol. 10, pp. 3459–3463, 2010.

[158] F. Meng, S. A. Morin, A. Forticaux, and S. Jin, "Screw dislocation driven growth of nanomaterials," *Accounts of Chemical Research*, vol. 46, pp. 1616–1626, 2013.

[159] P. E. Hopkins, J. C. Duda, S. P. Clark, C. P. Hains, T. J. Rotter, L. M. Phinney, and G. Balakrishnan, "Effect of dislocation density on thermal boundary conductance across GaSb/GaAs interfaces," *Applied Physics Letters*, vol. 98, p. 161913, 2011.

[160] Z. Su, L. Huang, F. Liu, J. P. Freedman, L. M. Porter, R. F. Davis, and J. A. Malen, "Layer-by-layer thermal conductivities of the Group III nitride films in blue/green light emitting diodes," *Applied Physics Letters*, vol. 100, no. 20, p. 201106, 2012.

[161] J. F. Ihlefeld, B. M. Foley, D. A. Scrymgeour, J. R. Michael, B. B. McKenzie, D. L. Medlin, M. Wallace, S. Trolier-McKinstry, and P. E. Hopkins, "Room temperature voltage tunable thermal conductivity via reconfigurable interfaces in ferroelectric thin films," *Nano Letters*, vol. 15, pp. 1791–1795, 2015.

[162] P. E. Hopkins, C. Adamo, L. Ye, B. D. Huey, S. R. Lee, D. G. Schlom, and J. F. Ihlefeld, "Effects of coherent ferroelastic domain walls on the thermal conductivity and Kapitza conductance in bismuth ferrite," *Applied Physics Letters*, vol. 102, no. 12, p. 121903, 2013.

[163] A. Mante and J. Volger, "The thermal conductivity of $BaTiO_3$ in the neighbourhood of its ferroelectric transition temperatures," *Physics Letters*, vol. 24A, pp. 139–140, 1966.

[164] K. J. Hubbard and D. G. Schlom, "Thermodynamic stability of binary oxides in contact with silicon," *Journal of Materials Research*, vol. 11, pp. 2757–2776, 1996.

[165] P. Scherrer, "Bestimmung der größe und der inneren struktur von kolloidteilchen mittels rööntgenstrahlen," *Nachrichten von der Gesellschaft der Wissenschaften zu Göttingen, Mathematisch-Physikalische Klasse*, vol. 1918, pp. 98–100, 1918.

[166] "Standard test methods for determining average grain size," 2014.

[167] M. S. O. Madelung, U. Rossler, *II-VI and I-VII Compounds; Semimagnetic Compounds*, vol. 41B, book section Magnesium oxide (MgO) crystal structure,

lattice parameters, thermal expansion, pp. 1–6. Heidelberg: Springer-Verlab GmbH, 1999.

[168] J. T. Luxon, D. J. Montgomery, and R. Summitt, "Effect of particle size and shape on the infrared absorption of magnesium oxides powders," *Physical Review*, vol. 188, pp. 1345–1356, 1969.

[169] Y. Touloukian and E. Buyco, *Thermophysical Properties of Matter - Specific Heat: Metallic Elements and Alloys*, vol. 4. New York: IFI/Plenum, 1970.

[170] G. S. Parks and K. K. Kelley, "The heat capacities of some metallic oxides," *Journal of Physical Chemistry*, vol. 30, pp. 47–55, 1926.

[171] A. Giri, J.-P. Niemela, T. Tynell, J. T. Gaskins, B. F. Donovan, M. Karppinen, and P. E. Hopkins, "Heat-transport mechanisms in molecular building blocks of inorganic/organic hybrid superlattices," *Phys. Rev. B*, vol. 93, p. 115310, Mar 2016.

[172] Y. S. Touloukian, R. W. Powell, C. Y. Ho, and P. G. Klemens, *Thermophysical Properties of Matter - Thermal Conductivity: Nonmetallic Solids*, vol. 2. New York, IFI/Plenum, 1970.

[173] D. T. Morelli and G. A. Slack, *High lattice thermal conductivity solids*, pp. 37–68. New York: Springer, 2006.

[174] G. Liebfried and E. Schlomann, "Wärmeleitung in elektrisch isolierenden kristallen," *Nachrichten der Akademie der Wissenschaften in Göttingen, Mathematisch-Physikalische Klasse*, vol. 4, no. 71, 1954.

[175] E. Grüneisen, "Theorie des festen zustandes einatomiger elemente," *Annalen der Physik*, vol. 344, no. 12, pp. 257–306, 1912.

[176] S.-M. Lee and D. G. Cahill, "Heat transport in thin dielectric films," *Journal of Applied Physics*, vol. 81, no. 6, pp. 2590–2595, 1997.

[177] A. Shah, P. Torres, R. Tscharner, N. Wyrsch, and H. Keppner, "Photovoltaic technology: The case for thin-film solar cells," *Science*, vol. 285, no. 5428, pp. 692–698, 1999.

[178] C. Ban, M. Xie, X. Sun, J. J. Travis, G. Wang, H. Sun, A. C. Dillon, J. Lian, and S. M. George, "Atomic layer deposition of amorphous TiO_2 on graphene as an anode for Li-ion batteries," *Nanotechnology*, vol. 24, no. 42, p. 424002, 2013.

[179] S. M. Lee, D. G. Cahill, and T. H. Allen, "Thermal conductivity of sputtered oxide films," *Physical Review B*, vol. 52, no. 1, pp. 253–257, 1995.

[180] J. M. Bennett, E. Pelletier, G. Albrand, J. P. Borgogno, B. Lazarides, C. K. Carniglia, R. A. Schmell, T. H. Allen, T. Tuttle-Hart, K. H. Guenther, and A. Saxer, "Comparison of the properties of titanium dioxide films prepared by various techniques," *Applied Optics*, vol. 28, no. 16, pp. 3303–3317, 1989.

[181] D. G. Cahill and T. H. Allen, "Thermal conductivity of sputtered and evaporated SiO_2 and TiO_2 optical coatings," *Applied Physics Letters*, vol. 65, no. 3, pp. 309–311, 1994.

[182] J. C. Lambropoulos, M. R. Jolly, C. A. Amsden, S. E. Gilman, M. J. Sinicropi, D. Diakomihalis, and S. D. Jacobs, "Thermal conductivity of dielectric thin films," *Journal of Applied Physics*, vol. 66, no. 9, p. 4230, 1989.

[183] D. Mergel, D. Buschendorf, S. Eggert, R. Grammes, and B. Samset, "Density and refractive index of TiO_2 films prepared by reactive evaporation," *Thin Solid Films*, vol. 371, no. 1–2, pp. 218–224, 2000.

[184] W. Yang and C. A. Wolden, "Plasma-enhanced chemical vapor deposition of TiO_2 thin films for dielectric applications," *Thin Solid Films*, vol. 515, no. 4, pp. 1708 – 1713, 2006.

[185] D. Samelor, A.-M. Lazar, M. Aufray, C. Tendero, L. Lacroix, J.-D. Beguin, B. Caussat, H. Vergnes, J. Alexis, D. Poquillon, N. Pebere, A. Gleizes, and C. Vahlas, "Amorphous alumina coatings: Processing, structure and remarkable barrier properties," *Journal of Nanoscience and Nanotechnology*, vol. 11, no. 9, pp. 8387–8391, 2011.

[186] J. K. Vohs, A. Bentz, K. Eleamos, J. Poole, and B. D. Fahlman, "Chemical vapor deposition of aluminum oxide thin films," *Journal of Chemical Education*, vol. 87, no. 10, pp. 1102–1104, 2010.

[187] Y. Balcaen, N. Radutoiu, J. Alexis, J.-D. Beguin, L. Lacroix, D. Samélor, and C. Vahlas, "Mechanical and barrier properties of MOCVD processed alumina coatings on Ti_6Al_4V titanium alloy," *Surface and Coatings Technology*, vol. 206, no. 7, pp. 1684 – 1690, 2011. Proceedings of the 38th International Conference on Metallurgical Coatings and Thin Films (ICMCTF)ICMCTF 2011The 38th International Conference on Metallurgical Coatings and Thin Films (ICMCTF).

[188] Y.-M. Lin, P. R. Abel, D. W. Flaherty, J. Wu, K. J. Stevenson, A. Heller, and C. B. Mullins, "Morphology dependence of the lithium storage capability and rate performance of amorphous TiO_2 electrodes," *The Journal of Physical Chemistry C*, vol. 115, no. 5, pp. 2585–2591, 2011.

[189] G. Dearnaley, A. M. Stoneham, and D. V. Morgan, "Electrical phenomena in amorphous oxide films," *Reports on Progress in Physics*, vol. 33, no. 3, p. 1129, 1970.

[190] M. R. Saleem, R. Ali, S. Honkanen, and J. Turunen, "Thermal properties of thin Al_2O_3 films and their barrier layer effect on thermo-optic properties of TiO_2 films grown by atomic layer deposition," *Thin Solid Films*, vol. 542, pp. 257–262, 2013.

[191] A. Cappella, J.-L. Battaglia, V. Schick, A. Kusiak, A. Lamperti, C. Wiemer, and B. Hay, "High temperature thermal conductivity of amorphous Al_2O_3 thin films grown by low temperature ALD," *Advanced Engineering Materials*, vol. 15, no. 11, pp. 1046–1050, 2013.

[192] G. N. Parsons, S. M. George, and M. Knez, "Progress and future directions for atomic layer deposition and ALD-based chemistry," *MRS Bulletin*, vol. 36, no. 11, p. 865–871, 2011.

[193] S. M. George, "Atomic layer deposition: An overview," *Chemical Reviews*, vol. 110, no. 1, pp. 111–131, 2010.

[194] R. L. Puurunen, "Surface chemistry of atomic layer deposition: A case study for the trimethylaluminum/water process," *Journal of Applied Physics*, vol. 97, no. 12, p. 121301, 2005.

[195] B. J. Nordell, T. D. Nguyen, C. L. Keck, S. Dhungana, A. N. Caruso, W. A. Lanford, J. T. Gaskins, P. E. Hopkins, D. R. Merrill, D. C. Johnson, L. L. Ross, P. Henry, S. W. King, and M. M. Paquette, "Conquering the low-k death curve: Insulating boron carbide dielectrics with superior mechanical properties," *Advanced Electronic Materials*, vol. 2, no. 7, pp. n/a–n/a, 2016.

[196] J. L. Braun, C. H. Baker, A. Giri, M. Elahi, K. Artyushkova, T. E. Beechem, P. M. Norris, Z. C. Leseman, J. T. Gaskins, and P. E. Hopkins, "Size effects on the thermal conductivity of amorphous silicon thin films," *Physical Review B*, vol. 93, no. 14, p. 140201, 2016.

[197] B. Shen, Z. Zeng, C. Lin, and Z. Hu, "Thermal conductivity measurement of amorphous Si/SiGe multilayer films by 3 omega method," *International Journal of Thermal Sciences*, vol. 66, pp. 19–23, 2013.

[198] M. Mazumder, T. Borca-Tasciuc, S. C. Teehan, E. Stinzianni, H. Efstathiadis, and S. Solovyov, "Temperature dependent thermal conductivity of Si/SiC amorphous multilayer films," *Applied Physics Letters*, vol. 96, no. 9, p. 093103, 2010.

[199] H.-S. Yang, D. G. Cahill, X. Liu, J. L. Feldman, R. S. Crandall, B. A. Sperling, and J. R. Abelson, "Anomalously high thermal conductivity of amorphous Si deposited by hot-wire chemical vapor deposition," *Physical Review B*, vol. 81, no. 10, p. 104203, 2010.

[200] X. Liu, J. L. Feldman, D. G. Cahill, R. S. Crandall, N. Bernstein, D. M. Photiadis, M. J. Mehl, and D. A. Papaconstantopoulos, "High thermal conductivity of a hydrogenated amorphous silicon film," *Physical Review Letters*, vol. 102, no. 3, p. 035901, 2009.

[201] B. L. Zink, R. Pietri, and F. Hellman, "Thermal conductivity and specific heat of thin-film amorphous silicon," *Physical Review Letters*, vol. 96, no. 5, p. 055902, 2006.

[202] C. D. Landon, R. H. T. Wilke, M. T. Brumbach, G. L. Brennecka, M. Blea-Kirby, J. F. Ihlefeld, M. J. Marinella, and T. E. Beechem, "Thermal transport in tantalum oxide films for memristive applications," *Applied Physics Letters*, vol. 107, no. 2, p. 023108, 2015.

[203] Z. C. Zhang, J. P. Roger, D. Fournier, A. C. Boccara, and J. C. Wang, "Thermal diffusivity of amorphous semiconductor superlattice films," *Thin Solid Films*, vol. 186, no. 2, pp. 361–366, 1990.

[204] S. W. King, J. Bielefeld, G. Xu, W. A. Lanford, Y. Matsuda, R. H. Dauskardt, N. Kim, D. Hondongwa, L. Olasov, B. Daly, G. Stan, M. Liu, D. Dutta, and D. Gidley, "Influence of network bond percolation on the thermal, mechanical, electrical and optical properties of high and low-k a-SiC:H thin films," *Journal of Non-Crystalline Solids*, vol. 379, pp. 67–79, 2013.

[205] D. B. Hondongwa, L. R. Olasov, B. C. Daly, S. W. King, and J. Bielefeld, "Thermal conductivity and sound velocity measurements of plasma enhanced chemical vapor deposited a-SiC:H thin films," *Thin Solid Films*, vol. 519, no. 22, pp. 7895–7898, 2011.

[206] R. M. Costescu, A. J. Bullen, G. Matamis, K. E. O'Hara, and D. G. Cahill, "Thermal conductivity and sound velocities of hydrogen-silsesquioxane low-k dielectrics," *Physical Review B*, vol. 65, no. 9, p. 094205, 2002.

[207] D. G. Cahill, M. Katiyar, and J. R. Abelson, "Thermal conductivity of *a*-Si:H thin films," *Physical Review B*, vol. 50, no. 9, pp. 6077–6081, 1994.

[208] P. E. Hopkins, B. Kaehr, E. S. Piekos, D. Dunphy, and C. Jeffrey Brinker, "Minimum thermal conductivity considerations in aerogel thin films," *Journal of Applied Physics*, vol. 111, no. 11, pp. 113532–113532–7, 2012.

[209] I. Stark, M. Stordeur, and F. Syrowatka, "Thermal conductivity of thin amorphous alumina films," *Thin Solid Films*, vol. 226, no. 1, pp. 185–190, 1993.

[210] S.-Y. Bai, Z.-A. Tang, Z.-X. Huang, J. Yu, and J.-Q. Wang, "Thermal conductivity measurement of submicron-thick aluminium oxide thin films by a transient thermo-reflectance technique," *Chinese Physics Letters*, vol. 25, no. 2, p. 593, 2008.

[211] S. Kawasaki, Y. Yamashita, N. Oka, T. Yagi, J. Jia, N. Taketoshi, T. Baba, and Y. Shigesato, "Thermal boundary resistance of W/Al_2O_3 interface in

$W/Al_2O_3/W$ three-layered thin film and its dependence on morphology," *Japanese Journal of Applied Physics*, vol. 52, no. 6R, p. 065802, 2013.

[212] N. Oka, R. Arisawa, A. Miyamura, Y. Sato, T. Yagi, N. Taketoshi, T. Baba, and Y. Shigesato, "Thermophysical properties of aluminum oxide and molybdenum layered films," *Thin Solid Films*, vol. 518, no. 11, pp. 3119–3121, 2010.

[213] R. Sultan, A. D. Avery, J. M. Underwood, S. J. Mason, D. Bassett, and B. L. Zink, "Heat transport by long mean free path vibrations in amorphous silicon nitride near room temperature," *Physical Review B*, vol. 87, no. 21, p. 214305, 2013.

[214] C. S. Gorham, J. T. Gaskins, G. N. Parsons, M. D. Losego, and P. E. Hopkins, "Density dependence of the room temperature thermal conductivity of atomic layer deposition-grown amorphous alumina Al_2O_3," *Applied Physics Letters*, vol. 104, no. 25, p. 253107, 2014.

[215] R. M. Costescu, D. G. Cahill, F. H. Fabreguette, Z. A. Sechrist, and S. M. George, "Ultra-low thermal conductivity in W/Al_2O_3 nanolaminates," *Science*, vol. 303, no. 5660, pp. 989–990, 2004.

[216] J.-P. Niemela, A. Giri, P. E. Hopkins, and M. Karppinen, "Ultra-low thermal conductivity in TiO_2:C superlattices," *Journal of Materials Chemistry A*, vol. 3, no. 21, pp. 11527–11532, 2015.

[217] S. W. Fong, A. Sood, L. Chen, N. Kumari, M. Asheghi, K. E. Goodson, G. A. Gibson, and H.-S. P. Wong, "Thermal conductivity measurement of amorphous dielectric multilayers for phase-change memory power reduction," *Journal of Applied Physics*, vol. 120, no. 1, p. 015103, 2016.

[218] M. A. Panzer, M. Shandalov, J. A. Rowlette, Y. Oshima, Y. W. Chen, P. C. McIntyre, and K. E. Goodson, "Thermal properties of ultrathin hafnium oxide

gate dielectric films," *IEEE Electron Device Letters*, vol. 30, no. 12, pp. 1269–1271, 2009.

[219] G. A. Slack, *The Thermal Conductivity of Nonmetallic Crystals*, vol. Volume 34, pp. 1–71. Academic Press, 1979.

[220] C. Kittel, "Interpretation of the thermal conductivity of glasses," *Physical Review*, vol. 75, no. 6, pp. 972–974, 1949.

[221] A. J. Bullen, K. E. O'Hara, D. G. Cahill, O. Monteiro, and A. von Keudell, "Thermal conductivity of amorphous carbon thin films," *Journal of Applied Physics*, vol. 88, no. 11, pp. 6317–6320, 2000.

[222] A. J. Griffin, F. R. Brotzen, and P. J. Loos, "The effective transverse thermal conductivity of amorphous Si_3N_4 thin films," *Journal of Applied Physics*, vol. 76, no. 7, pp. 4007–4011, 1994.

[223] O. W. Käding, H. Skurk, and K. E. Goodson, "Thermal conduction in metallized silicon-dioxide layers on silicon," *Applied Physics Letters*, vol. 65, no. 13, pp. 1629–1631, 1994.

[224] K. Bange, C. R. Ottermann, O. Anderson, U. Jeschkowski, M. Laube, and R. Feile, "Investigations of TiO_2 films deposited by different techniques," *Thin Solid Films*, vol. 197, no. 1, pp. 279–285, 1991.

[225] C. R. Ottermann and K. Bange, "Correlation between the density of TiO_2 films and their properties," *Thin Solid Films*, vol. 286, no. 1, pp. 32–34, 1996.

[226] C. Hu, M. Morgen, P. S. Ho, A. Jain, W. N. Gill, J. L. Plawsky, and P. C. Wayner, "Thermal conductivity study of porous low-k dielectric materials," *Applied Physics Letters*, vol. 77, no. 1, pp. 145–147, 2000.

[227] J. Fricke, X. Lu, P. Wang, D. Büttner, and U. Heinemann, "Optimization of monolithic silica aerogel insulants," *International Journal of Heat and Mass Transfer*, vol. 35, no. 9, pp. 2305–2309, 1992.

[228] K. E. Goodson, M. I. Flik, L. T. Su, and D. A. Antoniadis, "Annealing-temperature dependence of the thermal conductivity of LPCVD silicon-dioxide layers," *IEEE Electron Device Letters*, vol. 14, no. 10, pp. 490–492, 1993.

[229] A. J. Griffin, F. R. Brotzen, and P. J. Loos, "Effect of thickness on the transverse thermal conductivity of thin dielectric films," *Journal of Applied Physics*, vol. 75, no. 8, p. 3761, 1994.

[230] E. T. Swartz and R. O. Pohl, "Thermal resistance at interfaces," *Applied Physics Letters*, vol. 51, no. 26, p. 2200, 1987.

[231] G. Simmons and H. Wang, *Single Crystal Elastic Constants and Calculated Aggregate Properties*. Cambridge, MA: MIT, 1971.

[232] D. A. G. Bruggeman, "Berechnung verschiedener physikalischer konstanten von heterogenen substanzen. i. dielektrizitätskonstanten und leitfähigkeiten der mischkörper aus isotropen substanzen," *Annalen der Physik*, vol. 416, no. 7, pp. 636–664, 1935.